



## IL-10 protects against OPC ferroptosis by regulating lipid reactive oxygen species levels post stroke

Weihua Wu<sup>a,1</sup>, Zhaoli Luo<sup>a,1</sup>, Danmin Shen<sup>a</sup>, Ting Lan<sup>a</sup>, Zhongnan Xiao<sup>a</sup>, Meng Liu<sup>b</sup>, Liye Hu<sup>a</sup>, Tingting Sun<sup>a</sup>, Yamei Wang<sup>a</sup>, Jian-Nan Zhang<sup>b</sup>, Chenguang Zhang<sup>a</sup>, Peipei Wang<sup>b</sup>, Yabin Lu<sup>a</sup>, Fei Yang<sup>b,c,\*\*</sup>, Qian Li<sup>a,c,d,\*</sup>

<sup>a</sup> Department of Biochemistry and Molecular Biology, School of Basic Medical Sciences, Capital Medical University, Beijing, 100069, China

<sup>b</sup> Department of Neurobiology, School of Basic Medical Sciences, Capital Medical University, Beijing, 100069, China

<sup>c</sup> Laboratory for Clinical Medicine, Beijing Key Laboratory of Neural Regeneration and Repair, Capital Medical University, Beijing, 100069, China

<sup>d</sup> Beijing Key Laboratory of Cancer Invasion and Metastasis Research, Capital Medical University, Beijing, 100069, China

### ARTICLE INFO

#### Keywords:

Interleukin-10  
Oligodendrocyte progenitor cells  
Lipid reactive oxygen species  
Ferroptosis  
Intracerebral hemorrhagic stroke

### ABSTRACT

Accumulation of reactive oxygen species (ROS), especially on lipids, induces massive cell death in neurons and oligodendrocyte progenitor cells (OPCs) and causes severe neurologic deficits post stroke. While small compounds, such as deferoxamine, lipostatin-1, and ferrostatin-1, have been shown to be effective in reducing lipid ROS, the mechanisms by which endogenously protective molecules act against lipid ROS accumulation and subsequent cell death are still unclear, especially in OPCs, which are critical for maintaining white matter integrity and improving long-term outcomes after stroke. Here, using mouse primary OPC cultures, we demonstrate that interleukin-10 (IL-10), a cytokine playing roles in reducing neuroinflammation and promoting hematoma clearance, significantly reduced hemorrhage-induced lipid ROS accumulation and subsequent ferroptosis in OPCs. Mechanistically, IL-10 activated the IL-10R/STAT3 signaling pathway and upregulated the DLK1/AMPK/ACC axis. Subsequently, IL-10 reprogrammed lipid metabolism and reduced lipid ROS accumulation. In addition, in an autologous blood injection intracerebral hemorrhagic stroke (ICH) mouse model, deficiency of the endogenous *Il-10*, specific knocking out *Il10r* or *Dlk1* in OPCs, or administration of ACC inhibitor was associated with increased OPC cell death, demyelination, axonal sprouting, and the cognitive deficits during the chronic phase of ICH and *vice versa*. These data suggest that IL-10 protects against OPC loss and white matter injury by reducing lipid ROS, supporting further development of potential clinical applications to benefit patients with stroke and related disorders.

### 1. Introduction

Lipid metabolism reprogramming and reactive oxygen species (ROS) accumulation induce ferroptotic cell death in neurons, oligodendrocyte progenitor cells (OPCs), and cancer cells [1–3]. Among central nervous system diseases, intracerebral hemorrhagic stroke (ICH), caused by vascular rupture in the brain parenchyma, is a well-established disease model to study the regulatory mechanisms of lipid ROS in neural cells [2,4]. ICH accounts for 10% of all stroke types, but has a strikingly high rate of mortality and morbidity [5–7]. White matter (WM), consisting of axons connecting different brain regions, constitutes about half of the

total human brain volume [8], and loss of WM integrity is responsible for long-term functional and cognitive deficits in ICH [9]. Therefore, reducing WM damage and promoting WM repair may contribute to the ICH prognosis. However, current research mainly focuses on neuro-protective strategies, and largely neglects the protection of WM [10]. WM is comprised of axons, containing oligodendrocyte lineages (myelin-producing mature oligodendrocytes and OPCs) and other glial cells [8]. As central players in myelination and remyelination, the protection of oligodendrocytes and OPCs against cell death is essential for central nervous system activity [11]. Literature shows that autophagy is a key regulator of OPC survival during development [12], and OPC apoptosis

\* Corresponding author. Department of Biochemistry and Molecular Biology, School of Basic Medical Sciences, Capital Medical University, Beijing, 100069, China.

\*\* Corresponding author. Department of Neurobiology, School of Basic Medical Sciences, Capital Medical University, Beijing, 100069, China.

E-mail addresses: [feiyang@ccmu.edu.cn](mailto:feiyang@ccmu.edu.cn) (F. Yang), [qianli@ccmu.edu.cn](mailto:qianli@ccmu.edu.cn) (Q. Li).

<sup>1</sup> These authors contributed equally to this work.

is one of the most-studied etiologic mechanisms in WM injury (WMI)-related disorders such as multiple sclerosis (MS) [13,14]. Ferroptosis is a form of cell death caused by iron overload and abnormal cellular lipid metabolism [15]. Recent studies by our group and others have shown that OPCs undergo ferroptosis during hemorrhagic stroke, which accounts for a significant fraction of OPC loss in rodents [3,16]. Overwhelming oxidative stress due to intracellular iron overload and reduced activity of glutathione peroxidase 4 results in lipid peroxide accumulation and cell death [3,16]. In a mouse model of lateral ventricular hemorrhagic stroke, inhibition of OPC ferroptosis markedly improved axonal remyelination and neurobehavioral function [3]. However, our understanding of the underlying mechanisms of ferroptosis regulation in OPCs is still limited.

Interleukin-10 (IL-10) is an anti-inflammatory cytokine mainly produced by microglia and astrocytes in the brain, and the IL-10 receptor (mainly IL-10Ra) is widely expressed on various cell surfaces, including OPCs [17]. IL-10 is increased in serum, peripheral blood, and hematoma drainage fluid in patients with ICH, and IL-10 content is positively associated with the favorable outcomes [18]. Our previous work and others have shown that microglial IL-10 protects the brains of ICH mice by accelerating hematoma clearance [19,20]. These data suggest that IL-10 plays a beneficial role in the acute phase of ICH. Nevertheless, whether IL-10 affects chronic outcomes after ICH, which are strongly correlated with WMI severity and cognitive deficits, is largely unknown.

In animal disease models with critical demyelination, such as MS and premature brain injury, *Il-10*<sup>-/-</sup> mice exhibit more severe demyelination [21,22], and IL-10 administration increases the thickness of the myelin sheath and reduces WMI [22,23]. However, the underlying mechanism has not been identified and it remains unclear whether IL-10 affects the survival and differentiation of OPCs after ICH. The goal of this study was to better understand the role of the non-classical role of IL-10 in lipid ROS-induced WMI and its effect on the death and differentiation of OPCs during the chronic phase of ICH.

## 2. Materials and methods

### 2.1. Experimental design

All experiments were performed independently three or more times. The website ([www.randomization.com](http://www.randomization.com)) was applied to randomly assign animals or cell cultures to each group. Treatment, data collection, and data analyses were blinded by using different investigators or by masking sample labels. Experiments in animals were performed and reported according to the ARRIVE and ICLAS guidelines [24]. All procedures were approved by the Experimental Animal Ethics Committee of Capital Medical University. Anesthesia and euthanasia of animals were carried out based on American Veterinary Medical Association (AVMA) Guidelines for the Euthanasia of Animals (2020).

### 2.2. Animals

C57BL/6 mice (male, 6-8 weeks, 18-24 g) and neonatal mouse pups (P0-2, mixed genders) were purchased from Charles River Laboratories (Beijing, China). *Il-10*<sup>-/-</sup> mice (C57BL/6J background, #112663) were generated from Biocytogen (Beijing, China). PDGFR $\alpha$  Cre mice (C57BL/6J background, 018280) were purchased from Model Organisms Center, Inc. (Shanghai, China). Animals were housed under specific-pathogen-free conditions equipped with regulated temperature and illumination (room temperature [RT] 20  $\pm$  2  $^{\circ}$ C and 12-h light/dark cycle with lights on at 8:00 a.m.). Food (standard rodent laboratory chow, SPF-F02-001, SiPeiFu, China) and water were available ad libitum. All procedures and treatments were approved by the Animal Care and Use Committee of Capital Medical University.

### 2.3. ICH mouse model

Briefly [25], mice were anesthetized, and a burr hole was drilled (coordinate relative to bregma: x = 0.8 mm, y = 2.0 mm). Autologous blood (23  $\mu$ L) obtained from the mouse tail was infused in two-time blocks (z<sub>1</sub> = 2.9 mm, z<sub>2</sub> = 3.2 mm). Sham-operated mice received the same needle insertions.

### 2.4. Adeno-associated virus injection into striatum

The *Il-10ra* or *Dlk1* knockdown was using a pAAV-EF1a-DIO-mCherry plasmid (Obio Tech, Shanghai, China). The titers of virus particles were more than 1.0  $\times$  10<sup>12</sup> v.g./mL. The total of 4  $\times$  10<sup>9</sup> v.g./mL virus in 2  $\mu$ L was injected into 4 locations of striatum (Coordinates: x = 0.6 mm, y = 2.2 mm, z<sub>1</sub> = 3.05 mm/z<sub>2</sub> = 3.25 mm; x = 1.0 mm, y = 1.8 mm, z<sub>1</sub> = 3.05 mm/z<sub>2</sub> = 3.25 mm). 75 mg/kg tamoxifen dissolved in corn oil (T5648, Sigma, USA) was injected daily (*i.p.*) from 14 to 18 d after virus injection.

### 2.5. Cell culture

Mouse primary oligodendrocyte progenitor cells (OPCs) were prepared from neonatal mouse pups and cultured as described previously [3]. Briefly, brains of neonatal mouse pups (P0-1) were collected into cold Hank's buffer (H1045-500, Solarbio, China). The single cells generated from the cortex were isolated and processed with CD140 (PDGFR $\alpha$ ) MicroBead Kit (130-101-502, Miltenyi, USA). The PDGFR $\alpha$ <sup>+</sup> cells were then plated into Poly-DL-ornithine-coated (P0421, Sigma) culture plates and cultured in growth medium: DMEM/F12 (C11330500BT, Gibco, USA) with 2% B27 (17504044, Invitrogen, USA), 20 ng/mL PDGF-AA (100-13 A, PeproTech, USA), 20 ng/mL bFGF (100-18B, PeproTech), 1% penicillin-streptomycin (30-002-CI, Corning, USA) for 3 d before experiments.

To induce OPC differentiation, cells were treated with 50 ng/mL thyroid hormone (T3, T6397, Sigma) and 10 ng/mL ciliary neurotrophic factor (CNTF, 450-50, PeproTech). The medium was changed every 2 d.

OLN93 cells, an immortalized oligodendroglial cell line derived from neonatal rat brain [26], were cultured in DMEM medium (C11995500BT, Gibco) supplemented with 10% FBS and 1% penicillin/streptomycin, and passaged every other day.

### 2.6. Drug administration

Unless indicated specifically, we pretreated OPCs with recombinant murine IL-10 (2.5, 5, 10, 20, 40 ng/mL, 210-10, PeproTech) for 2 h. 50  $\mu$ M hemin (16009-13-5, Frontier Scientific, USA), ND-646 (0.5, 5, 10 nM, HY-101842, MedChemExpress, USA), 10  $\mu$ M AG490 (HY-12000, MedChemExpress), 2.5  $\mu$ M Stattic (S7024, Selleck, USA) and 100  $\mu$ M Deferoxamine (DFO, Y0001937, Sigma) were administrated on OPCs for 12 h.

To intracerebroventricularly administrate drugs into ICH mice, we fixed microtube (62001, RWD, China) on the skull (coordinate relative to bregma: x = 0.8 mm, y = 0.5 mm). 10  $\mu$ g/kg IL-10 in ddH<sub>2</sub>O, 10 mM AG490 in 0.1% DMSO, 1  $\mu$ M ND-646 (1  $\mu$ L) in 0.1% DMSO and vehicle were injected at 0, 2, 4, 6 d after ICH.

### 2.7. Cell death detection

For *in vitro* experiments, cells were incubated with 100 ng/mL Propidium Iodide (PI, P4170, Sigma) for 30 min, and images were taken using a fluorescence microscope (Nikon ECLIPSE Ti, Japan). At least 3 microscopic fields were captured and evaluated for each well. Three wells were assigned to one group and served as an independent test. Cell death was calculated as the percentage of PI<sup>+</sup> cells.

*In vivo*, cell death was detected with a TUNEL assay kit (C1088, C1090, Beyotime, China), according to the manufacturer's instructions. Sections were permeabilized by 0.3% (v/v) Triton X-100 and then

incubated with a TUNEL reaction mixture for 1 h at 37 °C. The treated slices were incubated with anti-PDGFR $\alpha$  (3174, Cell Signaling Technology, USA) and then Alexa Fluor 488 goat-anti-rabbit IgG (A-11008, Invitrogen). Images were obtained by a fluorescence microscope (Nikon ECLIPSE Ci) or confocal microscope (TCS SP8 STED, Leica, Germany). At least three microscopic fields surrounding lesion were captured in each section. Three sections, at the sites of anterior, middle and posterior of the hematoma, were chosen for each mouse. TUNEL and PDGFR $\alpha$  double immunopositively cells were counted.

## 2.8. Lipid peroxidation measurements

BODIPY<sup>TM</sup> 581/591C11 is a currently major assay used to measure lipid peroxidation in ferroptosis [27]. Cells were incubated with 10  $\mu$ M BODIPY<sup>TM</sup> 581/591C11 reagent (D3861, Invitrogen) for 30 min at 37 °C as previously reported [3]. The cellular fluorescence was detected by a fluorescence microscope (Nikon ECLIPSE Ti) or flow cytometry (LSR Fortessa SORP, BD, USA) using 590 nm and 510 nm channels. Results were analyzed by BD FACSDiva<sup>TM</sup> and FlowJo v10 (BD).

## 2.9. MDA measurement

As previously reported [25], cells were prepared in Malondialdehyde (MDA) Lysis Buffer with BHT (K739-100, Biovision, USA), and then centrifuged at 13000 g for 10 min. Thiobarbituric acid reagent was added into each vial including standards and samples. Pipette 200  $\mu$ L from each reaction mixture into a 96-well microplate for analysis. The absorbance at 532 nm was recorded and calculated according to the manufacturer's instructions.

## 2.10. Reverse transcription-quantitative PCR (RT-qPCR) and RNA-seq

The mRNA was extracted with TRIzol (15596018, Invitrogen) and cDNA was obtained by performing reverse transcription with Reverse Transcriptase kit (R323-01, Vazyme, China). qPCR was performed with the PowerUp<sup>TM</sup> SYBR<sup>TM</sup> Green Master Mix (A25742, Applied Biosystems, USA) by 7500 Fast Real-Time PCR System (Applied Biosystems 7500). Primers were as follows: *GAPDH* (Forward 5'-TGGATTGGACGCATTGGTC-3', Reverse 5'-TTTGCACTGGTACGTGTTGAT-3'); *Hmox1* (Forward 5'-AAGCCGAGAATGCTGAGTTCA-3', Reverse 5'-GCCGTGATGATATGGTACAAGGA-3'); *Hamp1* (Forward 5'-CTTGCCAGCCTGAGCAGCACCTAT-3', Reverse 5'-AGAGAGGTCAGGATGTGGCTCTAGGCTATG-3'); *Slc7a11* (Forward 5'-GGCACCGTCATCGGATCAG-3', Reverse 5'-CTCCACAGGACAGACAGAAA-3'); *Acs14* (Forward 5'-CTCACCATATATTGCTGCCTGT-3', Reverse 5'-TCTCTTTGCCATAGCGTTTTTCT-3'); *MnSOD* (Forward 5'-CAGACCTGCCTTACGACTATGG-3', Reverse 5'-CTCGGTGGCGTTGAGATTGT-3'); *IL-10* (Forward 5'-GCTCTTACTGACTGGCATGAG-3', Reverse 5'-CGCAGCTCTAGGAGCATGTG-3'); *Dlk1* (Forward 5'-CTGGCTTCTCAGGCAACTTCTGT-3', Reverse 5'-CAGCTCC TCGCCGCTGTTAT-3'); *Sox10* (Forward 5'-ACACCTTGGGACACGGT TTTC-3', Reverse 5'-TAGGTCTTGTTCCTCGGCCAT-3'); *Nkx2.2* (Forward 5'-CCGGGCGGAGAAAGGTATG-3', Reverse 5'-CTGTAGCGGAAAAGGGA-3'); *Olig2* (Forward 5'-TCCCAGAACCCGATGATCTT-3', Reverse 5'-CGTGACGAGGACACAGTC-3'); *Ascl1* (Forward 5'-GCAACCGGGTCAAGTTGGT-3', Reverse 5'-GTCGTTGGAGTAGTTGGG-3'); *Bmp2* (Forward 5'-GGGACCCGCTGTCTTAGT-3', Reverse 5'-TCAACTCAAAT TCGCTGAGGAC-3'); *Myrf* (Forward 5'-GCATGGGCACCGCCCTAAG-3', Reverse 5'-GGGGCGAGTCTGGCAGTGTG-3'); *Bmp6* (Forward 5'-AGAA GCGGGAGATGCAAAAGG-3', Reverse 5'-GACAGGGCGTTGTAGAGATC C-3'); *Dlk1* (-1390 to -1174 bp) (Forward 5'-GGCTGCAAGCACCTTACC-3', Reverse 5'-GCTTAGAGGATGGGAGTGGG-3'); *IL10ra* (Forward 5'-CCCATTCTCTCAGCATCTC-3', Reverse 5'-TCAGACTGGTTTGGGATAGGTTT-3').

For DNA electrophoresis experiment, the end products of RT-qPCR were separated with agarose gel electrophoresis and visualized by gel imaging system (Gel Doc XR System, Bio-Rad, USA).

RNA-Seq analysis was performed with the Illumina HiSeq platform to identify the differential expression genes [3]. Briefly, mRNAs were enriched with Oligo-d(T) beads and reverse transcribed into cDNA. After the construction of the library, the libraries were sequenced by Illumina HiSeq sequencer (PE 150, USA). FASTQ reads were trimmed and required a minimum length of 20 bp. After filtering, the clean reads were aligned to the reference genome using Hierarchical Indexing, after which gene expression levels were quantified. The screened differentially expressed genes were analyzed by Gene Ontology (GO) function analysis (<http://metascape.org>), Kyoto Encyclopedia of Genes and Genomes (KEGG) pathway function analysis, hierarchical clustering analysis, and volcano plot analysis. The primary sequencing data have been deposited in the NCBI Gene Expression Omnibus (GEO, <https://www.ncbi.nlm.nih.gov/geo/>) under accession number GSE222049.

## 2.11. Lipidomic analysis

OLN93 cells were treated with vehicle, 50  $\mu$ M hemin, 50  $\mu$ M hemin + 10 ng/mL IL-10, 50  $\mu$ M hemin + 5 nM ND-646 for 12 h. Cells were digested and collected in 60% methyl alcohol (diluted with water, containing 8.5 g/L ammonium bicarbonate). The suspensions were centrifuge to remove supernatant. Cells were then frozen in liquid nitrogen and stored at -80 °C. The subsequent operations were provided by Shanghai Biotree Biotech. Briefly, LC-MS/MS analyses were performed using an UHPLC system (Vanquish, Thermo Fisher Scientific), equipped with a Kinetex C18 column (2.1 x 100 mm, 1.7  $\mu$ m, Phenomen). The QE mass spectrometer was used for its ability to acquire MS/MS spectra on data dependent acquisition (DDA) mode in the control of the acquisition software (Xcalibur 4.0.27, Thermo).

## 2.12. ChIP assay

Briefly [25], OLN93 cells ( $5 \times 10^6$ ) were fixed with 1% (w/v) formaldehyde solution at 37 °C for 10 min, followed by treated with ultrasonic and incubated with p-STAT3 (9145T, Cell Signaling Technology) or IgG (C1755, Appligen, China) antibodies at 4 °C overnight. The antibody-protein-DNA complex was immunoprecipitated with protein A/G (sc-2003, Santa Cruz, USA), washed and eluted sequentially. After decrosslinking, DNA was extracted with PCR Purification Kit (28106, QIAquick, Germany). qPCR and DNA electrophoresis experiments were subsequently performed.

## 2.13. Western blotting

The protein was extracted with RIPA Lysis buffer (AR0101, Boster, China) mixed with protease inhibitor cocktail (04693132001, Roche, USA). Cell culture medium was collected, and the protein in cell supernatant was concentrated with centrifugal filter devices for 30 min at 7500 g (UFC201024, Millipore, USA). Samples were separated by sodium dodecyl sulfate-polyacrylamide gel electrophoresis and then transferred onto polyvinylidene fluoride membrane (1620177, Bio-rad). Membranes were blocked with 5% (w/v) nonfat milk and incubated with antibodies listed as follows: IL-10 (1:1000, ab9969, Abcam, USA), p-STAT3 (1:1000, 9145T, Cell Signaling Technology), STAT3 (1:1000, ET1607-38, Huabio, China), p-STAT1 (1:1000, 7649, Cell Signaling Technology), STAT1 (1:1000, 14994, Cell Signaling Technology), p-STAT5 (1:1000, 4322, Cell Signaling Technology), STAT5 (1:1000, 94205, Cell Signaling Technology), p-ACC (1:1000, 3661S, Cell Signaling Technology), ACC (1:1000, 21923-1-AP, Proteintech, USA), DLK1 (1:1000, ab210471, Abcam), AMPK (1:1000, 5832S, Cell Signaling Technology; 1:1000, ab32047, Abcam), p-AMPK (1:1000, 2535S, Cell Signaling Technology),  $\beta$ -actin (1:2000, sc-47778, Santa Cruz), anti-rat IgG, HRP-linked Antibody (7077S), anti-rabbit IgG, HRP-linked Antibody (7071S), anti-mouse IgG, HRP-linked Antibody (7076S) (1:1000, Cell Signaling Technology). Protein bands were visualized after incubating chemiluminescent HRP substrate (90719, Millipore) with the

Fusion system (Odyssey SA, Vilber, France). The relative intensity was quantified with ImageJ software (NIH, USA).

#### 2.14. Immunofluorescence staining

Animals were euthanized and perfused with PBS and 4% (w/v) paraformaldehyde (158127, Sigma). Coronal sections (16  $\mu$ m) of brains blocked by 5% (v/v) goat serum were incubated with primary antibodies and corresponding secondary antibodies. Antibodies used were as follows: anti-MBP (sc271524, Santa Cruz), anti-NF200 (N0142, Sigma), anti- $\beta$ -APP (51-2700, Invitrogen), anti-Caspr (MABN69, Millipore), anti-Nav1.6 (ASC-009, Alomone, Jerusalem), anti-PDGFR $\alpha$  (3174, Cell Signaling Technology), anti-Olig2 (ab9610, Millipore), Alexa Fluor 594 goat-anti-rabbit IgG (A-11012, Invitrogen), Alexa Fluor 594 goat-anti-mouse IgG (A-11005, Invitrogen), Alexa Fluor 488 goat-anti-rabbit IgG (A-11008, Invitrogen) and Alexa Fluor 488 goat-anti-mouse IgG (A-11001, Invitrogen). Images were obtained by fluorescence microscope (Nikon ECLIPSE Ci) or confocal microscope (TCS SP8 STED, Leica). At least three microscopic fields around the lesion were captured in each section. Three sections, at the sites of anterior, middle and posterior of the hematoma, were chosen for each mouse. Data were analyzed by an investigator who was blinded to the experimental setup.

#### 2.15. Injection and staining of BrdU

As previously reported [28], mice were intraperitoneally injected with the thymidine analogue BrdU (50 mg/kg, B9285, Sigma) twice a day for 4 d, beginning at 3 d after ICH. Brain slices were treated with 2 N HCl for 60 min at RT to partially denaturalize the double-stranded DNA, and followed with 0.1 M boric acid (pH 8.5) for 15 min. The sections were incubated with anti-BrdU (ab6326, Abcam) and anti-APC (OP80, Millipore) overnight at 4  $^{\circ}$ C, then with Alexa Fluor 594 goat anti-Rat IgG (A-11007, Invitrogen) and Alexa Fluor 488 goat-anti-mouse IgG (A-11001, Invitrogen). Images were obtained by a fluorescence microscope (Nikon ECLIPSE Ci). At least three microscopic fields surrounding the lesion were captured in each section. Three sections, at the sites of anterior, middle and posterior of the hematoma, were selected for each mouse. BrdU and APC double immunopositive cells were counted by an investigator blinded to the experimental setup.

#### 2.16. Anterograde axonal tracing

At 21 d after ICH, 2  $\mu$ L of BDA (10%, w/v, dissolved in PBS, D1956, Thermo Fisher Scientific) were injected into the contralateral cortex at two sites ( $x_1 = 0.6$  mm,  $y_1 = 1.2$  mm,  $z_1 = 1.5$  mm;  $x_2 = 0.0$  mm,  $y_2 = 1.8$  mm,  $z_2 = 1.7$  mm). 14 d later, slices were collected at the levels of facial nucleus (FN) and 7th segment of cervical spinal cord (C7) (35  $\mu$ m thick), and incubated with Streptavidin-FITC (S3762, Sigma) to label BDA<sup>+</sup> axons. Images were obtained by a fluorescence microscope (Nikon ECLIPSE Ci). Three sections at each level were selected for each mouse. The number of midline-crossing BDA<sup>+</sup> fibers was quantified [29,30].

#### 2.17. Luxol fast blue staining

The integrity of myelin sheath is detected by Luxol fast blue staining as previously reported [2]. Slices were pretreated with 70% ethanol overnight at RT and then incubated with prewarmed Luxol fast blue solution (L0294, Sigma) overnight at 37  $^{\circ}$ C. Brain sections were dehydrated, fixed with xylene and then sealed with sealing agent. Three sections, at the sites of anterior, middle and posterior of the hematoma, were selected for each mouse and the intensity of fast blue in the striatum was quantified using ImageJ software. Data were analyzed by an investigator who was blinded to the experimental setup.

#### 2.18. MRI

As previously reported [3], mice were anesthetized with isoflurane, and maintained at  $\sim$ 50 breaths per minute. Magnetic resonance imaging (MRI) was performed by Bruker Biospin 11.7 T MR scanner (Germany). Diffusion tensor imaging (DTI) was performed by using a three-segments diffusion-weighted echo-planar imaging sequence. The following parameters were used: echo time = 19 ms, repetition time = 1500 ms, averages = 1, b value = 1500 s/mm<sup>2</sup>, the field of view was 15  $\times$  15 mm, slice thickness = 0.5 mm. The FA value was measured with MATLAB software (MathWorks, USA) by a blinded investigator.

#### 2.19. TEM assay

As previously reported [3], mice were intracardially perfused with PBS, 4% PFA and 2.5% glutaraldehyde (Top0394, Biotopped, China). Tissue blocks (1 mm<sup>3</sup>) were microdissected from corpus callosum and striatum, and fixed in 2.5% glutaraldehyde for 24 h. Furthermore, samples were fixed in 1% osmium tetroxide (00308, TCI, Japan) for 2 h and then dehydrated in ethanol and acetone. Samples embedded in epoxy resin were cut into ultrathin sections, stained with uranyl acetate (SPI-02624, HEAD BIO, China) and lead citrate (HD17800, HEAD BIO). Fields randomly selected in corpus callosum and striatum were obtained with TEM (JEM-1400plus). The G-ratio, a parameter of myelination, was calculated and analyzed with the ImageJ software.

#### 2.20. Gait analysis assay

The CatWalk XT<sup>®</sup> assay is used to sensitively and unbiasedly assess small changes in motor function, and the CatWalk XT apparatus (Noldus Information Technology, The Netherlands) was used as previously described [31]. During the training period, the mice were allowed to traverse the plate to their home cages 3 times over 3 d. Data recorded on the last day was used as a baseline before surgery. At 35 d after ICH, the mice were allowed to complete 3 trials. Investigator blinded to the groups analyzed the parameters of contralateral paws by CatWalk XT 10.6 software.

#### 2.21. Novel object recognition test

Novel object recognition test reflects cognitive function [32]. Mice were allowed to acclimate for 30 min and then placed into the chamber with 2 identical cube objects (5 cm in size) for 5 min. Afterwards, the cube object was replaced by a new rectangular pyramid. In the novel object testing phase, the mice were allowed to explore for 10 min. Object investigations consisted of all exploratory tries, including sniffing and biting, but not sitting on the object, or casually touching the object in passing. Animals that spent less than 20 s exploring novel objects were excluded from the analysis. The percentage of novel object recognition time to total exploration time was counted [33].

#### 2.22. Forced swimming test

Mice were allowed to acclimate for 30 min and then placed into plastic cylinders (height, 30 cm; diameter, 20 cm) containing water (25  $\pm$  1  $^{\circ}$ C; depth, 15 cm) for 5 min [34]. The immobility time during forced swimming was scored by an investigator who was blinded to the groups.

#### 2.23. Tail suspension test

After acclimating for 30 min, mice were suspended using adhesive tape (approximately 1 cm from the tip of the tail), and the tape was hooked at the top of the box [34]. The tip of mouse's nose was approximately 20 cm away from the floor. The mice were suspended for 5 min, and the immobility time was scored by a blinded investigator.

## 2.24. Open field test

Mice were allowed to acclimate for 30 min and then placed in the center of a white plastic chamber (50 cm × 50 cm × 50 cm) to explore freely for 5 min [35]. The tracks were recorded and analyzed by an investigator blinded to groups.

## 2.25. Neurologic and motor function evaluations

Briefly, body symmetry, gait, climbing, circling behavior, front limb symmetry, and compulsory circling were scored as reported [2,25]. Each score was graded on a scale from 0 to 4. In forelimb placement tests, intact mice would quickly place the lateral forelimb on the tabletop as a

response to the whisker stimulation. The percentage of successful responses in 10 trials was quantified by an investigator blinded to groups.

## 2.26. Statistical analysis

Values were shown as mean ± SD. Statistical analysis was performed using unpaired two-tailed student's *t*-test for two groups, One-way ANOVA followed by Tukey's or Dunnett's multiple comparisons test, and Two-way ANOVA followed by Tukey's multiple comparisons test for multiple groups (GraphPad Prism 7.0 Software).  $p < 0.05$  was considered significant.

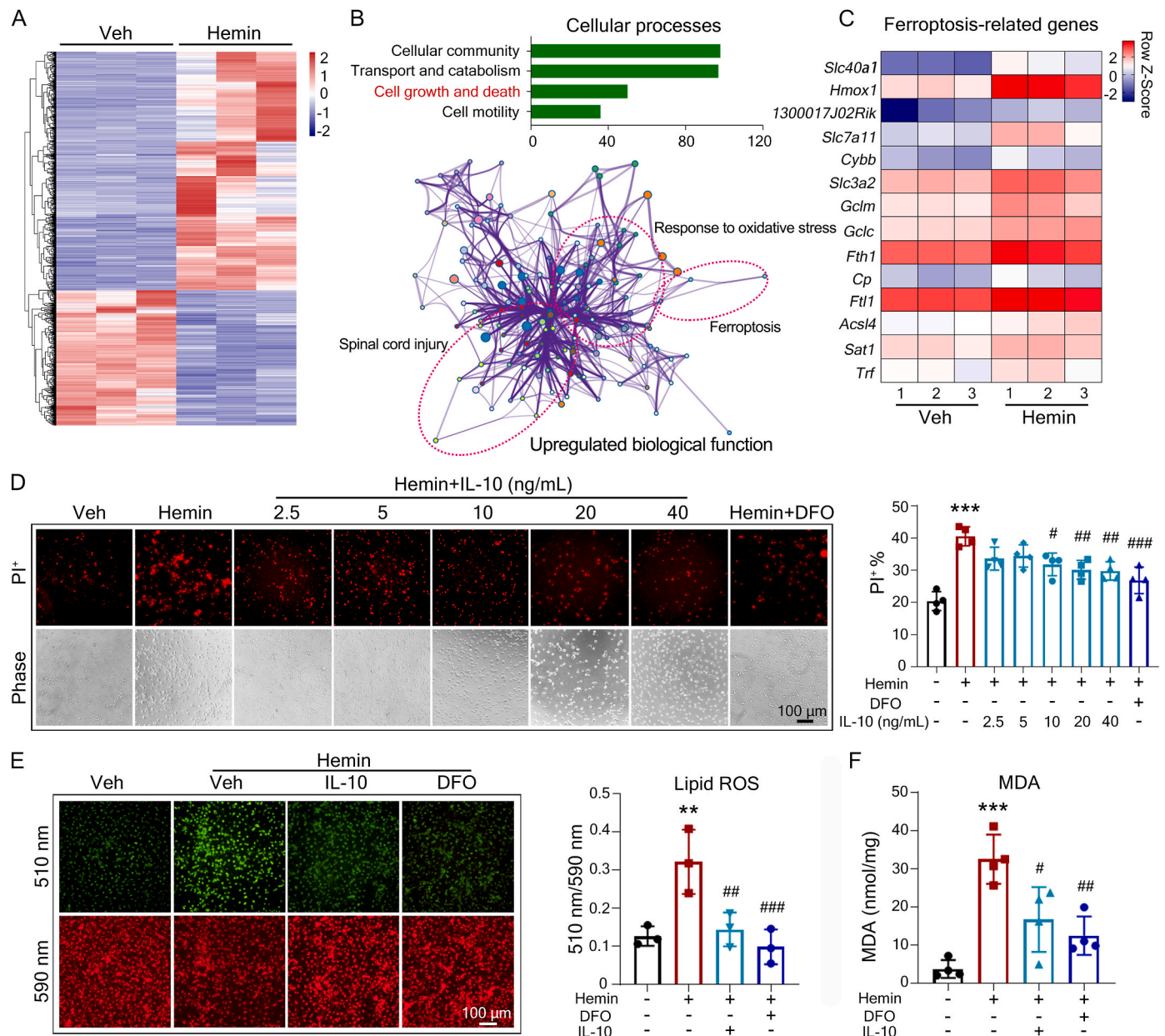


**Fig. 1.** IL-10 reverses OPC ferroptosis induced by hemin. (A–C) Mouse primary OPCs were isolated and treated with vehicle or hemin for 12 h. RNA-seq analysis was performed. Hierarchical clustering of differently expressing genes (DEGs, fold change threshold >2; FDR-corrected  $p < 0.05$ ) is shown (A). KEGG pathway and GO enrichment analysis are shown (B). The genes related to ferroptosis among DEGs are shown in the heatmap (C). (D) OPCs were pretreated with IL-10 for 2 h before incubating with hemin for 12 h. The representative images of PI staining and quantification are shown. (E, F) OPCs were treated as indicated for 12 h. Lipid ROS and MDA content were measured using BODIPY-C11 probe (E) and an MDA detective kit (F). Results are presented as scatter plots (mean ± SD). (D–F) One-way ANOVA followed Tukey's multiple comparisons test. \*\* $p < 0.01$ , \*\*\* $p < 0.001$  vs vehicle; # $p < 0.05$ , ## $p < 0.01$ , ### $p < 0.001$  vs hemin. Each experiment was repeated 3 or 4 times independently except the RNA-seq analysis. Scale bars: (D, E) 100 μm.

### 3. Results

#### 3.1. IL-10 decreases lipid ROS and protects against ferroptosis in OPCs

Hemin is a degradation product of red blood cells, and has been commonly used to mimic ICH toxicity and to induce OPC ferroptosis *in vitro* [3,25,36]. To understand the molecular regulatory mechanism in OPC cell death post-ICH, we extracted primary OPCs from mouse pups, cultured them, and treated them with hemin or vehicle. RNA-seq analysis was performed and 3014 differentially expressed genes between hemin- and vehicle-treated cells were identified (Fig. 1A and Table S1). The Kyoto encyclopedia of genes and genomes (KEGG) analysis identified that the genes related to cell growth and death dramatically changed after hemin treatment (Fig. 1B). The gene ontology (GO) enrichment was further processed among upregulated genes (fold change >3) and the network plot represented the relationships between the main regulated biological processes, including response to oxidative stress, ferroptosis, and spinal cord injury (Fig. 1B). Ferroptosis is a cell death form caused by iron overload and abnormal cellular lipid metabolism. Consistent with our previous data that ferroptosis is the predominant cell death form in OPC cell death after hemorrhagic stroke, 14 ferroptosis-related genes were found to be notably changed in hemin-treated OPCs by RNA-seq analysis (Fig. 1C). To investigate whether IL-10 affected to the OPC ferroptosis, we incubated primary OPCs with different concentrations of recombinant IL-10 under hemin stimulation. Pretreating of IL-10 (10 ng/mL) successfully rescued hemin-induced ferroptosis in OPCs, as effective as the ferroptosis inhibitor deferoxamine (DFO) (Fig. 1D). In keeping with this result, hemin-induced accumulation of lipid ROS and polyunsaturated fatty acid peroxidation end product malondialdehyde (MDA), the hallmarks of ferroptosis, were reduced significantly by the addition of IL-10

(Fig. 1E and F). These data suggest that IL-10 protected against OPC ferroptosis induced by hemin *in vitro*.

#### 3.2. IL-10 rescues OPC ferroptosis by activating IL-10Ra/STAT3 signaling pathway and transcribing *Dlk1*

IL-10 binds to the IL-10 receptor (mainly IL-10Ra) and translocates STAT1/3/5 into the nucleus [37]. We confirmed the expression of IL-10Ra in OPCs (Figs. S1A and B), which was consistent with the previous report [17]. Compared to the hemin group, IL-10 increased p-STAT3 (Tyr705) level, which was completely abolished by the inhibitors of STAT3 signaling pathway, AG490 and Stattic (Fig. 2A), whereas IL-10 did not change p-STAT1 (Tyr701) or p-STAT5 (Tyr694) in OPCs (Figs. S1C and D). Consistent with this, the p-STAT3 level also dramatically increased in the ipsilateral striata at 1 and 3 d after ICH *in vivo*, which was corresponding to the elevated IL-10 protein levels (Fig. 2B). In addition, AG490 and Stattic also abolished the effects of IL-10 on lipid ROS accumulation (Fig. 2C) and cell death (Fig. 2D) in hemin-treated OPCs. These data indicate that IL-10 rescued hemin-induced ferroptosis in OPCs through activation of the STAT3 signaling pathway, but not through the STAT1/5 signaling pathway.

To investigate how IL-10/STAT3 rescued OPC ferroptosis, we examined the expression levels of characterized ferroptosis-related genes transcribed by transcription factor STAT3 in other cells and disease models [38–42]. Unexpectedly, compared with hemin, IL-10 did not change the expression of *MnSOD*, *Hmox1*, *Hamp*, *Slc7a11*, or *Acsf4* in hemin-induced ferroptotic OPCs (Figs. S1E–I), indicating that IL-10/STAT3 rescued OPC ferroptosis not by regulating established targets. RNA-seq analysis was further carried out, and co-administration of hemin and IL-10 significantly altered the expression of 61 genes compared with hemin treatment alone, with 6 upregulated and 55

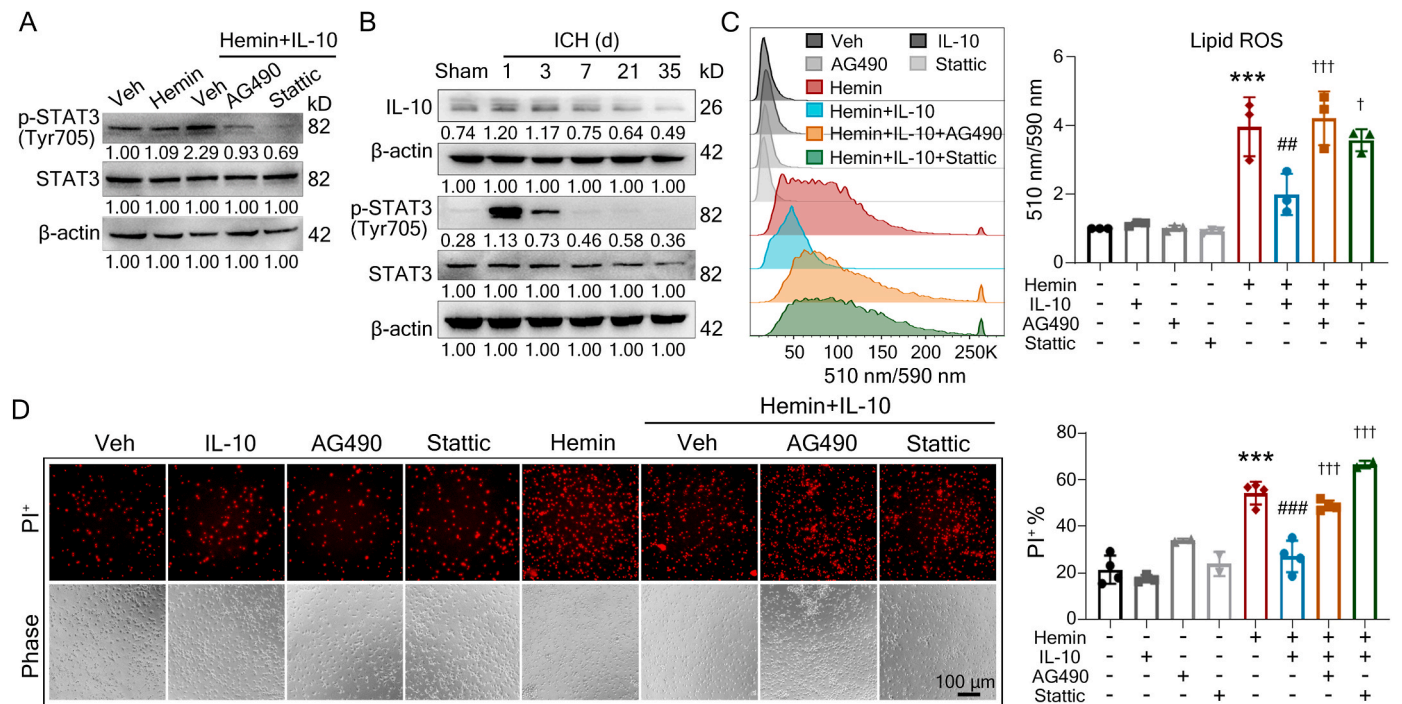


**Fig. 2. IL-10 activates STAT3 to rescue OPC ferroptosis.** (A) OPCs were treated as indicated and the p-STAT3 was analyzed using Western blotting.  $\beta$ -actin served as an internal control. Representative images and quantification are presented. (B) Autologous blood was injected into striata of wildtype (WT) mice. The ipsilateral striata brain tissue samples or corresponding sham brain samples were collected at indicated time post-surgery. The levels of STAT3, p-STAT3, and IL-10 were quantified using Western blotting.  $\beta$ -actin served as an internal control. Representative images and quantification are presented. (C) OPCs were treated as indicated for 12 h and labeled with BODIPY-C11 probe. Lipid ROS was detected with flow cytometry. Representative histogram images of fluorescence and quantification are shown. (D) OPCs were treated as indicated for 12 h before performing PI staining. The representative images and quantification are shown. Results are presented as scatter plots (mean  $\pm$  SD). (C, D) One-way ANOVA followed Tukey's multiple comparisons test. \*\*\* $p$ <0.001 vs vehicle; ## $p$ <0.01, ### $p$ <0.001 vs hemin; † $p$ <0.05, ††† $p$ <0.001 vs hemin + IL-10. Each experiment was repeated 3 or 4 times independently. Scale bar: (D) 100  $\mu$ m.

downregulated genes (Fig. 3A and Table S2). *Dlk1* was the gene with the most dramatic increase among these (Fig. 3A and Table S2). Of note, *Dlk1* was also significantly down-regulated in hemin-treated cells compared with vehicle-treated cells, revealed by RNA-seq analysis (Fig. S2A and Table S1).

*Dlk1* encoding protein delta-like 1 homolog (DLK1) belongs to the epidermal growth factor-like repeat-containing family, and is considered as a preadipocyte factor with an impact on adipogenesis and metabolism, exerting effects in membrane form or soluble form [43]. We additionally verified the RNA-seq data with RT-qPCR. Hemin-decreased *Dlk1* expression was reversed by IL-10 administration, and STAT3 inhibitor Stattic effectively abolished the effect of IL-10 on *Dlk1* expression (Fig. 3B). DNA gel electrophoresis followed by RT-qPCR identified that *Dlk1* isoform 1 was the isoform regulated by the IL-10/STAT3 signaling pathway (Fig. 3C and D). Additionally, our chromatin immunoprecipitation (ChIP) assay verified that IL-10 induced the binding of p-STAT3 to the promoter region of *Dlk1* (Fig. 3E).

To further explore whether DLK1 served as a key regulator in IL-10-rescued OPC ferroptosis, we knocked down the expression of *Dlk1* with shRNA lentiviruses (Fig. S2B). Compared with control shRNA treatment, knocking down *Dlk1* effectively reversed the protective effects of IL-10 on ferroptotic OPCs as determined by lipid ROS (Fig. 3F) and cell death (Fig. 3G) assays. In addition, we concentrated cell supernatants and performed Western blotting. It showed DLK1 expression existed in the cell lysate but not in the cell supernatant (Fig. S2C), suggesting that the membrane form of DLK1 rescued OPC ferroptosis, but not the cleaved DLK1 in the medium.

### 3.3. IL-10 inhibits ACC activity via DLK1 and regulates lipid metabolism in OPCs

Ferroptosis is primarily driven by iron-dependent phospholipid peroxidation, and the KEGG analysis revealed that the genes related to lipid metabolism dramatically changed in hemin-treated OPCs

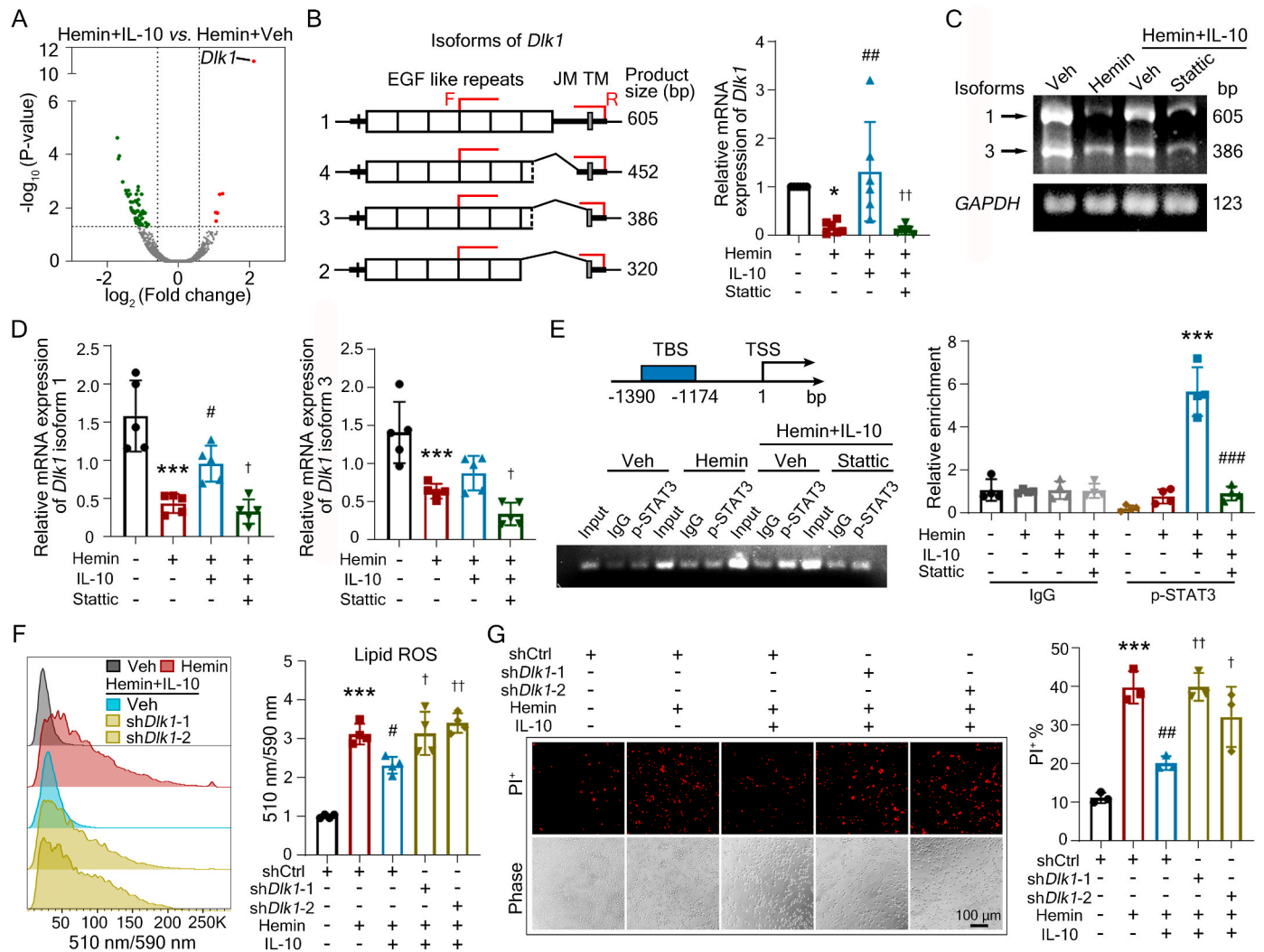


**Fig. 3. IL-10 activates STAT3 and transcribes *Dlk1* to rescue OPC ferroptosis.** (A) OPCs were treated as indicated and RNA-seq was performed. DEGs are shown in volcano plot (fold change threshold >1.5; FDR-corrected  $p < 0.05$ ). (B-D) Schematic diagram shows structures of *Dlk1* isoforms and the sites of consensus primers. OPCs were treated as indicated and the mRNA levels of *Dlk1* was detected by RT-qPCR (B) and DNA gel electrophoresis (C, D). *GAPDH* served as the internal control. JM, juxtamembrane domain; TM, transmembrane domain. (E) OLN93 cells (rat OPCs) were treated as indicated and ChIP assay was performed using p-STAT3 antibodies. The location of primer is shown. Agarose gel electrophoresis and qPCR were performed following ChIP assay. TBS, transcription factor binding site. TSS, transcription start site. (F, G) OPCs were infected with sh*Dlk1* or control vector. After 2 d, OPCs were treated as indicated. Lipid ROS was labeled with BODIPY-C11 fluorescence probe and then detected by flow cytometry (F). Cell death rate was quantified with PI staining (G). Results are presented as scatter plots (mean  $\pm$  SD). (B, D, F, G) One-way ANOVA followed Tukey's multiple comparisons test. (E) Two-way ANOVA followed Tukey's multiple comparisons test. \* $p < 0.05$ , \*\*\* $p < 0.001$  vs corresponding vehicle (B, D, F, G) or hemin (E); # $p < 0.05$ , ## $p < 0.01$ , ### $p < 0.001$  vs corresponding hemin (B, D, F, G) or hemin + IL-10 (E); † $p < 0.05$ , †† $p < 0.01$  vs corresponding hemin + IL-10 (B, D, F, G). Each experiment was repeated 3-6 times independently. Scale bar: (G) 100  $\mu$ m.

(Fig. S2D). Acetyl-CoA carboxylase (ACC) is the key enzyme that catalyzes the acetyl-CoA to malonyl-CoA and functions to promote fatty acid synthesis and also inhibits fatty acid oxidation [44]. Phosphorylation of ACC (p-ACC) on serine 79 (Ser79) inhibits its activity and protects against ferroptosis in mouse embryonic fibroblasts [44], and DLK1 inhibits ACC activity in hepatocytes [45]. Therefore, we hypothesized that IL-10/STAT3/DLK1 regulated ACC activity and lipid metabolism in ferroptotic OPCs.

Hemin decreased the levels of DLK1, p-AMPK, and p-ACC in the OPCs (Fig. 4A). IL-10 reversed hemin-decreased p-ACC levels (Fig. 4A), and the addition of Stattic or knocking down of *Dlk1* abolished the effects of IL-10 on hemin-incubated OPCs (Fig. 4A-C). We further treated OPCs with ND-646, the specific inhibitor of ACC, and found it protected against hemin-induced lipid ROS accumulation and ferroptosis dose-dependently as IL-10 and DLK1 did (Fig. 4D and E). We next performed untargeted lipidomic analyses (FDR-corrected  $p < 0.05$ ; variable Importance in the Projection, VIP > 1). Hemin increased the contents of triacylglycerol (TAG) and phosphatidylcholine (PC) in OPCs, while hemin plus IL-10 or ND-646 treatment significantly reduced the contents of TAG, phosphatidylglycerol (PG), phosphatidylethanolamine (PE), and PC (Fig. 4F). There were 37 significantly changed lipid metabolites among the pairwise comparisons of three groups, including fatty acid (FA) (16:1), PC (14:0e/22:4), PC (16:0e/20:4), PC (16:1e/20:4), PC (16:0e/22:2), PC (16:0e/24:1), PC (16:1e/22:3), PC (18:1e/20:2), PC (18:1e/21:2), PC (18:2e/22:1), PC (18:4e/21:2), PC (18:3e/18:0), PC (16:0e/24:4), PE (16:0e/20:4), PE (18:2e/22:4), PE (16:1e/22:5), PE (22:3e/16:2), and PG(16:0/18:0) (Fig. 4G and H). IL-10 and ND-646 treatment both decreased these metabolites levels (Fig. 4G and H), which is consistent with the current consensus that the oxidation of polyunsaturated fatty acid (PUFA)-containing phospholipids drives ferroptosis [46,47]. These results suggest that IL-10 downregulated ACC activity and inhibited ferroptosis in OPCs by modulating lipid metabolism.

### 3.4. IL-10-rescued ferroptotic OPCs preserves the ability of differentiation

The differentiation and maturation of OPCs into myelinating oligodendrocytes is a critical process in the therapeutic strategy for ICH [48]. To verify whether IL-10-rescued ferroptotic OPCs preserved the ability to differentiate into myelin-producing oligodendrocytes, OPCs were cultured in differentiation medium (containing differentiation factors thyroid hormone (T3) and ciliary neurotrophic factor (CNTF)) and treated with hemin. Persistently exposure of hemin with lower concentrations significantly abolished OPCs differentiation (Fig. 5A-C), as quantified with the percentage of myeline binding protein (MBP)<sup>+</sup> oligodendrocytes. IL-10 successfully increased the absolute number of Olig2<sup>+</sup> (total number of cells) and MBP<sup>+</sup> cells (mature oligodendrocytes) (Fig. 5D and E), but failed to rescue the hemin-inhibited OPCs differentiation rate (the percentage of MBP<sup>+</sup> cells) (Fig. 5B and C). Short exposure of 50 μM hemin (EC50) to OPCs also showed similar results (Figs. S3A-C). We further examined the mRNA expression levels of well-established differentiation-related genes, and IL-10 failed to reverse the hemin-induced expression changes of differentiation-inhibiting genes (*Bmp2* and *Bmp6*) or differentiation-promoting genes (*Sox10*, *Nkx2.2*, *Olig2*, *Ascl1*, and *Myrf*) as well (Fig. 5F). Of note, addition of IL-10 remarkably promoted differentiation in naive OPCs (Figs. S3D and E). The above results suggest that IL-10 failed to reverse the hemin-inhibitory effects on differentiation, but was able to maintain the differentiation ability of surviving OPCs.

### 3.5. Deficiency of endogenous IL-10 increases OPC cell death, reduces newborn oligodendrocytes, and exacerbates WMI post-ICH in vivo

To explore the role of IL-10 in the chronic phase of ICH mice, we developed global *IL-10* knockout mice using the CRISPER/Cas9 technique. We injected autologous blood into *IL-10*<sup>-/-</sup> mice and WT

littermates, and characterized the cell death and differentiation of OPCs at different time points post-ICH. We stained brain sections with OPC marker alpha-type platelet-derived growth factor receptor (PDGFRα) and the bona fide cell death staining dye terminal deoxynucleotidyl transferase mediated dUTP nick end labeling (TUNEL) [49,50]. We observed the increased percentage of TUNEL<sup>+</sup>PDGFRα<sup>+</sup> cells in *IL-10*<sup>-/-</sup> mice at 7 d after ICH in the surrounding lesion area, indicating a severe OPC loss in *IL-10* deficiency mice compared to WT mice (Fig. 6A). We next injected 5-bromo-2'-deoxyuridine (BrdU) to ICH mice and labeled the newborn oligodendrocytes (Fig. 6B). Compared to WT mice, the numbers of BrdU<sup>+</sup>APC<sup>+</sup> and APC<sup>+</sup> cells were decreased in *IL-10*<sup>-/-</sup> mice, indicating that endogenous IL-10 was indispensable to maintain newly-differentiated mature oligodendrocytes post-ICH (Fig. 6C).

To determine whether deficiency of endogenous IL-10 resulted in aggravated WMI after ICH, we firstly assessed brain injuries with magnetic resonance imaging (MRI) in *IL-10*<sup>-/-</sup> and WT littermates post-ICH. Diffusion tensor imaging (DTI) detects the magnitude and directionality of water molecules within fiber tracts, and provides parameters of myelin sheath integrity [51,52]. Compared with the WT group, the fractional anisotropy (FA) value of ipsilateral corpus callosum (CC) was markedly lower in *IL-10*<sup>-/-</sup> mice at 5 d and 35 d after ICH (Fig. 6D), reflecting the more severe injury of ipsilateral fiber tracks. No difference in the FA value of contralateral CC between the two groups was noticed (Fig. S4A). In addition, we performed classic histochemical staining, and found that *IL-10*<sup>-/-</sup> mice exhibited decreased intensity of Luxol fast blue staining in the ipsilateral hemisphere (Fig. S4B). We next performed immunofluorescence staining using different markers for assessing myelin sheath integrity (MBP<sup>+</sup>), axonal damage (β-APP<sup>+</sup>/NF200<sup>+</sup>), and the number of Ranvier nodes (Caspr and Nav1.6). *IL-10*<sup>-/-</sup> mice showed significant loss of myelin sheath integrity (Fig. 6E), aggravated axonal damage (Figs. S4C-E), and decreased number of Ranvier nodes (Fig. S4F) in the ipsilateral hemisphere. We further used transmission electron microscopy (TEM) to examine the ultrastructure of axons and myelin sheath. We found that the myelin thickness (G-ratio) was also additionally increased in the ipsilateral external callosum (EC) and striatum in *IL-10*<sup>-/-</sup> ICH mice, indicating a thinner thickness of myelin (Fig. 6F-H). Of note, the significant differences in myelin thickness between WT and *IL-10*<sup>-/-</sup> ICH mice were in axons with smaller diameters (Fig. 6H).

To further investigate the effects of IL-10 on the neuroplasticity, we injected tract-tracer biotinylated dextran amine (BDA) into the contralateral cortex at 21 d after ICH [29,30], and quantified the number of BDA<sup>+</sup> axons crossing the midline at levels of the facial nuclei and the 7th cervical spinal cord segment at 35 d after ICH (Fig. S5A). The number of BDA<sup>+</sup> fibers crossing the midline at each level was notably decreased in WT ICH mice, and further diseased in *IL-10*<sup>-/-</sup> ICH mice (Figs. S5B-D). These results suggest that endogenous IL-10 is essential for the protection against WMI in the chronic phase after ICH.

Considering WM plays a critical role in executive function [53], cognition [33], and emotion [54,55], we next evaluated behavioral changes in *IL-10*<sup>-/-</sup> and control ICH mice. The neurologic/motor dysfunction of WT ICH mice recovered along with time (Figs. S5E and F), and displayed similar paw print lengths of contralateral forelimbs and hindlimbs, and displayed no significant changes compared with sham-operated mice at 35 d post-ICH which were assessed with the CatWalk XT® system, while *IL-10*<sup>-/-</sup> mice showed a significant reduction in paw print lengths of limbs (Fig. 6I). In novel object tests, *IL-10* deficiency markedly decreased the ratio of exploration time spent to the total exploration time, suggesting an aggravated cognitive deficit compared with WT mice (Fig. 6J). In addition, forced swimming test (FST), tail suspension test (TST), and open field test (OFT) were conducted to assess the emotional changes among groups [56-58]. *IL-10*<sup>-/-</sup> mice exhibited longer immobility times relative to WT mice in both FST and TST tests (Figs. S5G and H), but showed no difference in the exploration time spent on central region in OFT (Fig. S5I).

The above results suggest that endogenous IL-10 is indispensable to

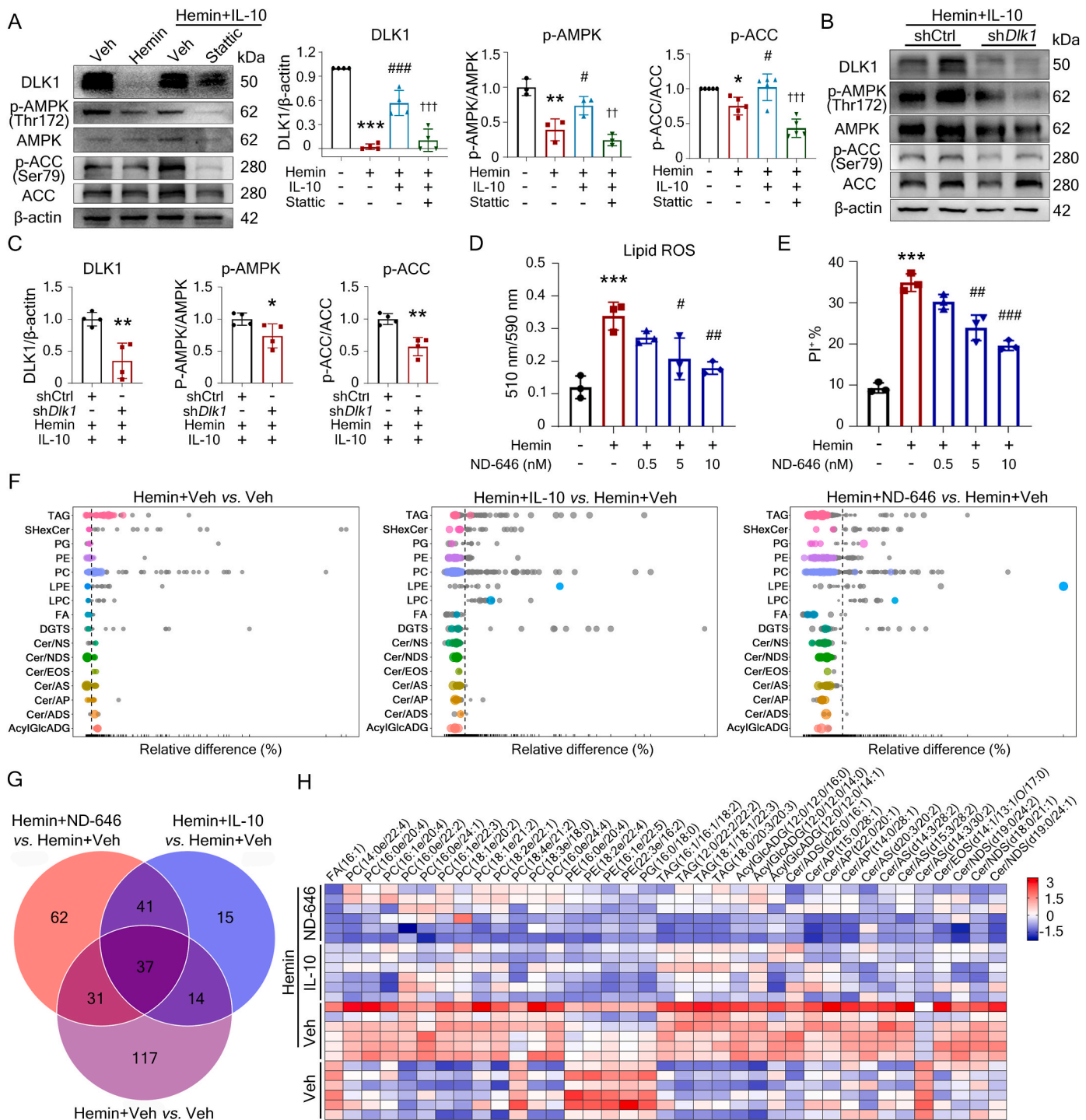


**Fig. 4. IL-10/STAT3/DLK1 inhibits ACC activity and regulates lipid metabolism in OPCs.** (A–C) OPCs were infected with *shDlk1* lentiviruses or control. Then cells were treated as indicated and the expressions of DLK1, AMPK, p-AMPK, ACC, and p-ACC in the cell lysate were detected using Western blotting. β-actin served as an internal control. The representative images and quantifications are shown. (D, E) OPCs were treated as indicated. The accumulations of lipid ROS (D) and cell death rate (E) were detected. Quantification is shown. (F–H) OLN93 cells (rat OPCs) were treated as indicated for 12 h. Cells were collected and untargeted lipidomic analyses were performed (FDR-corrected  $p < 0.05$ ; Variable Importance in the Projection,  $VIP > 1$ ). The common differential expression of metabolic species among 3 comparisons are shown as bubble plots (F). Venn diagram shows the significantly changed lipid metabolites in 3 groups (G). Heat map of 37 significantly changed lipid metabolites is shown (H). TAG, triacylglycerol; SHexCer, sulfurHexosylceramide hydroxyfatty acid; PG, phosphatidylglycerol; PE, phosphatidylethanolamine; PC, phosphatidylcholine; LPE, lysophosphatidylethanolamine; LPC, lysophosphatidylcholine; FA, free fatty acid; DGTS, diacylglycerol trimethylhomoserine; Cer/NS, ceramide non-hydroxyfatty acid-sphingosine; Cer/NDS, ceramide non-hydroxyfatty acid-dihydro-sphingosine; Cer/EOS, ceramide esterified omega-hydroxy fatty acid-sphingosine; Cer/AS, ceramide alpha-hydroxy fatty acid-sphingosine; Cer/AP, ceramide alpha-hydroxy fatty acid-phytospingosine; Cer/ADS, ceramide alpha-hydroxy fatty acid-dihydro-sphingosine; AcylGlcADG, acylglucuronosyldiacylglycerol. Results are presented as scatter plots (mean ± SD). (A, D, E) One-way ANOVA followed Tukey’s multiple comparisons test. (C) Unpaired two-tailed student’s *t*-test. \* $p < 0.05$ , \*\* $p < 0.01$ , \*\*\* $p < 0.001$  vs corresponding vehicle (A, D, E) or shCtrl + hemin + IL-10 (C); # $p < 0.05$ , ## $p < 0.01$ , ### $p < 0.001$  vs corresponding hemin (A, D, E); † $p < 0.01$ , †† $p < 0.001$  vs hemin + IL-10 (A). Each experiment was repeated 3–5 times independently.

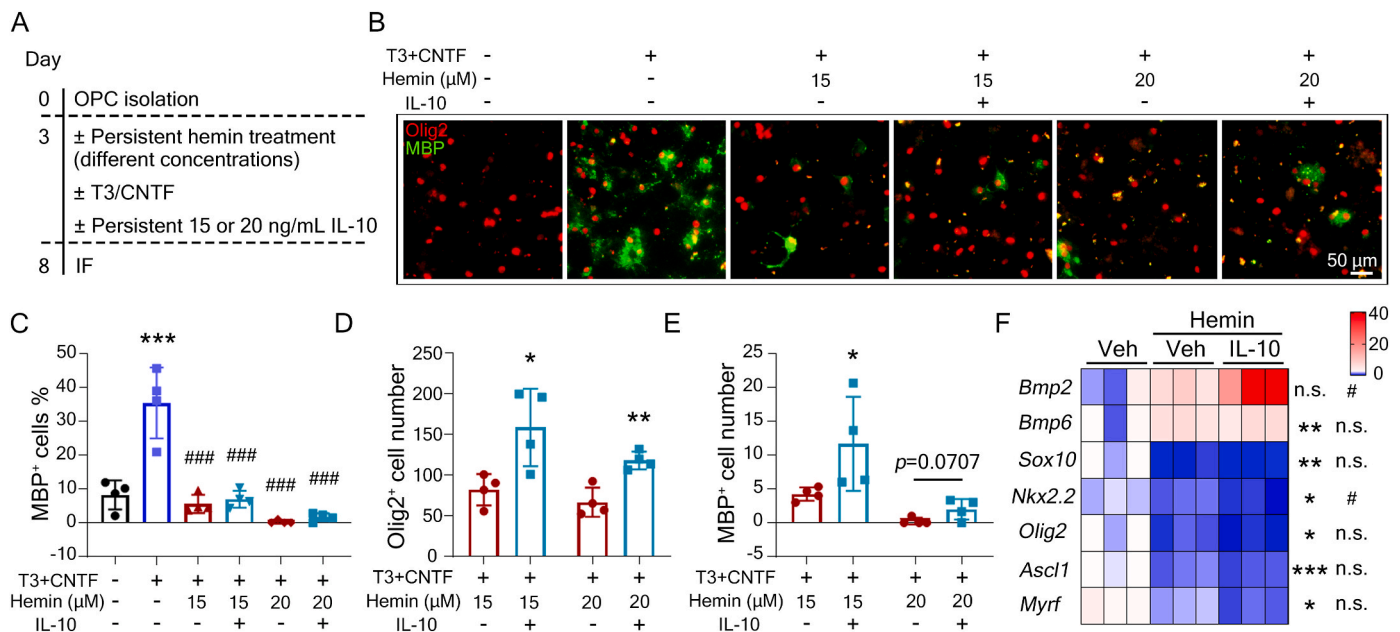


**Fig. 5.** IL-10-rescued OPCs have capacity to differentiate into mature oligodendrocytes. (A–E) OPCs were treated as indicated and performed immunofluorescence staining using Olig2 and MBP antibodies. Schematic experimental procedure (A), representative images (B), quantifications of the differentiation rate (C), Olig2<sup>+</sup> cell number (D), and MBP<sup>+</sup> cell number (E) are shown. (F) OPCs were treated as indicated for 12 h before performing RT-qPCR. The expressions of differentiation-inhibiting genes (*Bmp2*, *Bmp6*) and differentiation-promoting (*Sox10*, *Nkx2.2*, *Olig2*, *Ascl1*, *Myrf*) genes are shown in the heatmap. *GAPDH* served as an internal control. Results are presented as scatter plots (mean ± SD). (C, F) One-way ANOVA followed Tukey's multiple comparisons test. (D, E) Two-tailed student's *t*-test followed by Welch's correction. \**p*<0.05, \*\**p*<0.01, \*\*\**p*<0.001 vs vehicle (C, F) or T3 + CNTF + hemin (D, E); #*p*<0.05, ##*p*<0.001 vs T3 + CNTF (C) or hemin (F). n.s., not significant. Each experiment was repeated 3 or 4 times independently. Scale bar: (B) 50 μm.

protect OPCs from cell death and to maintain the pool of oligodendrocytes during the chronic phase of ICH. Moreover, IL-10 is necessary to protect against WMI, benefits axonal sprouting, motor function and cognitive function, and improves depressive-like behaviors post-ICH.

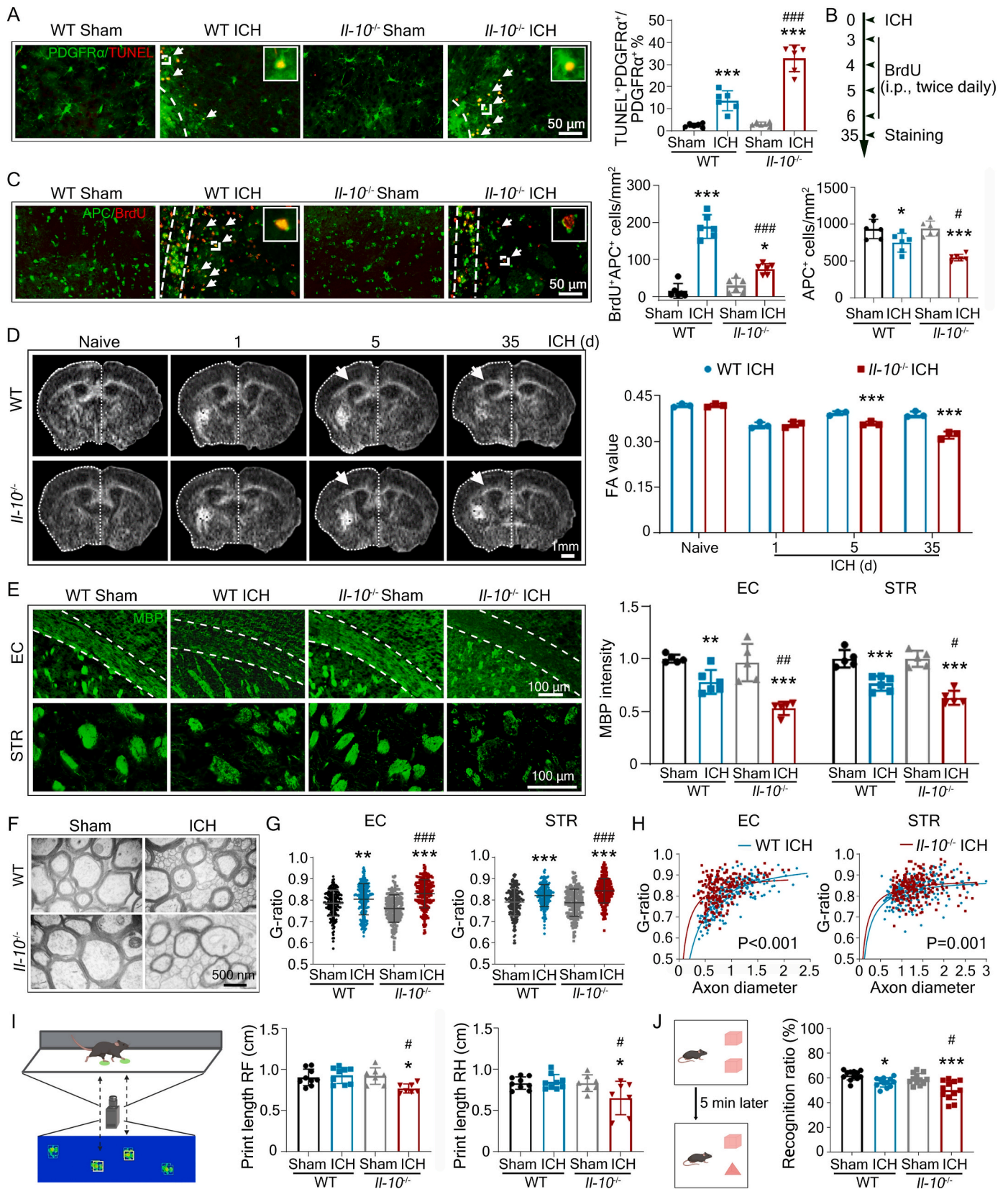
### 3.6. IL-10 treatment rescues OPC ferroptosis, maintains oligodendrocytes number, and improves cognitive function

To define the therapeutic effects of IL-10 and further confirm the protective effects of IL-10 was through regulating IL-10Ra/STAT3/DLK1/ACC axis *in vivo*, we administrated IL-10, AG490, or ND-646 to the WT ICH mice, or injected pAAV-EF1a-DIO-mCherry virus (a Cre enzyme-initiated virus) to PDGFRα Cre mice to deplete *Il-10ra* or *Dlk1* in striatal OPCs. Both IL-10 and ND-646 significantly protected against OPC cell death, while AG490 eliminated the protective effect of IL-10, as shown the changed percentage of TUNEL<sup>+</sup>PDGFRα<sup>+</sup> cells in the surrounding lesion area at 7 d after ICH (Fig. 7A). Knocking out *Il-10ra* or *Dlk1* expression in striatal OPCs abolished the effects of IL-10 on OPC cell death markedly (Fig. 7B–D). Consistent with this, administration of IL-10 or ND-646 resulted in more newly-differentiated oligodendrocytes and total number of mature oligodendrocytes, while the effect of IL-10 was abolished by AG490 injection, indicated by changed numbers of BrdU<sup>+</sup>APC<sup>+</sup> and APC<sup>+</sup> cells compared with vehicle treated mice at 35 d after ICH (Fig. 7E and F). Lossing of *Il-10ra* or *Dlk1* expression in OPCs reversed the progress of OPCs differentiation exerted by IL-10 treatment (Fig. 7G and H). Additionally, both IL-10 and ND-646 treatment rescued cognitive impairment of WT ICH mice, while AG490 abolished IL-10 effects significantly (Fig. 7I). And knocking out *Il-10ra* or *Dlk1* expression in OPCs also eliminated the enhancement on cognitive function exerted by IL-10 treatment (Fig. 7J). These results show that IL-10 treatment protects against OPC ferroptosis and improves cognitive function through IL-10 receptor/STAT3/DLK1 axis after ICH *in vivo*.

## 4. Discussion

ICH is the second most common type of stroke, associated with the highest mortality and disability [59]. Cell death of neurons and oligodendroglial lineages induced by inflammatory, oxidative, and cytotoxic cascades result in severe WMI and functional impairment [60]. Importantly, OPCs reprogram their lipid metabolism and change their membrane composition progressively during developing, increasing the biosynthesis of cholesterol and galactosphingolipids and reducing the relative amounts of phospholipids and proteins [61]. Considering the highest iron content, the lower contents of antioxidant agents (e.g., glutathione peroxidase), and only half of the glutathione reductase activity compared with other glial cells, the oligodendroglial lineage is the most vulnerable cell class to oxidative stress [62]. Recently, we and others have found that ferroptosis, an iron-dependent cell death characterized by disturbance of lipid metabolism and accumulation of lipid peroxidation, in OPCs contributes greatly to neurologic deficits after hemorrhagic damage [2,3,63]. Mitochondria, organelles containing oxidized lipid subcellular membranes, also play a major role in ferroptosis [64]. Several studies have shown the mitochondria can act as initiators or amplifiers of ferroptosis initiated by cysteine starvation and glutathione depletion [65,66]. Nevertheless, the regulatory mechanism for ferroptosis in OPCs remains unclear post-ICH. In this study, we found that the expression of IL-10 was protectively elevated during the acute phase of ICH. Elevated IL-10 decreased lipid ROS and protected against OPCs ferroptosis, thus replenishing the mature oligodendrocyte pool and accelerating the WMI recovery during the chronic phase after ICH.

The IL-10 serves multiple functions in the central nervous system, including limiting neuroinflammation, enhancing microglia phagocytosis, regulating neuronal activity, and promoting neurogenesis [17,19,67,68]. It is reported that IL-10 benefits hemorrhagic brain by inhibiting apoptosis, accelerating hematoma clearance, and restraining inflammation [19,69,70]. In other diseases, studies have shown that IL-10 protects against apoptosis of retinal ganglion cells induced by withdrawing growth factors via phosphorylating STAT3 [71], and inhibits



(caption on next page)

**Fig. 6. Deficiency of IL-10 increases OPC cell death, reduces oligodendrocyte pool, and exacerbates WMI post-ICH.** Male *Il-10*<sup>-/-</sup> and WT littermates (6–8 weeks old) underwent autologous intrastriatal blood injection or sham procedure. (A) Brain sections obtained at 7 d post-ICH were stained with PDGFR $\alpha$  and TUNEL. Representative images and quantification are shown. White dash lines indicate the ipsilateral lesion area. White arrows indicate double-positively stained cells. (B, C) Sections obtained at 35 d post-ICH were stained with BrdU and APC. Experimental procedures (B), representative images (C), and quantifications (C) are shown. White dash lines indicate the lesion area. White arrows indicate double-positively stained cells. (D) MRI was performed before and after ICH at indicated time points. Representative diffusion tensor images and quantification of FA values of the ipsilateral corpus callosum are shown. White arrows indicate ipsilateral corpus callosum. (E) Brain sections obtained at 35 d post-ICH were stained with MBP. Representative images and quantifications are shown. White dash lines indicate the ipsilateral corpus callosum region. (F–H) Brain sections obtained at 35 d post-ICH were observed with transmission electron microscopy (TEM). Representative images and G-ratio of axons are shown. (I) Motor functions of ICH mice were assessed with a CatWalk XT<sup>®</sup> apparatus at 35 d post-ICH in WT and *Il-10*<sup>-/-</sup> mice. A schematic diagram of recorded footprints and representative images of footprints are shown. The lengths of right forelimb (RF) and right hindlimb (RH) were quantified. (J) Cognitive function of WT and *Il-10*<sup>-/-</sup> mice were measured at 35 d post-ICH with novel object recognition test. Illustrating diagram of the test and the percent times spent on the novel object over the total between groups are shown. Results are presented as scatter plots (mean  $\pm$  SD) except H (line chart). (A, C–E, G, I, J) Two-way ANOVA followed Tukey's multiple comparisons test. (H) Nonparametric test, Mann-Whitney test. \* $p$ <0.05, \*\* $p$ <0.01, \*\*\* $p$ <0.001 vs corresponding sham (A, C, E, G, I, J) or WT ICH (D). # $p$ <0.05, ## $p$ <0.001, ### $p$ <0.001 vs corresponding ICH (A, C, E, G, I, J). Each group contained 5–6 (A, C, E), 3 (D, G, H), or 7–10 (I, J) animals. Axons calculated for evaluating G-ratio: WT sham  $n$  = 205, WT ICH  $n$  = 223, *Il-10*<sup>-/-</sup> sham  $n$  = 216, *Il-10*<sup>-/-</sup> ICH  $n$  = 210 (G, H). Scale bars: (A, C) 50  $\mu$ m, (D) 1 mm, (E) 100  $\mu$ m, (F) 500 nm.

oligodendrocyte cell death caused by LPS/IFN- $\gamma$  cytotoxicity through suppressing the expression of inducible nitric oxide synthase [72]. Additionally, in MS and premature brain injury, IL-10 shows WM protective effects by reducing inflammatory response or collagen I synthesis [21–23]. In this study, we specifically knocked out the expression of *IL-10ra* in OPCs and elucidated the direct function of IL-10 on OPCs. To the best of our knowledge, this study is the first to show that IL-10 decreased lipid ROS in OPCs and plays a protective role in WMI after ICH.

STAT3 is the direct downstream of multiple interleukin factors, including IL-10 and IL-6 [37,73]. Phosphorylation of Tyr705 at STAT3 leads to its activation and nuclear translocation [74]. STAT3 signaling pathway plays a key role in repressing ROS/lipid ROS production [38–42,75], regulating cell differentiation and neurogenesis [68,76], and preventing cell death (including cancer cell ferroptosis) [41,52,71]. Consistent with these findings, we confirmed that IL-10-inhibited ferroptosis depends on STAT3 activation in OPCs, but not on STAT1/5. Unexpectedly, we did not find any change in expression of previously reported STAT3-transcribed genes between the hemin and hemin + IL-10 groups. These data implied the existence of novel target genes of STAT3 that were peculiar to the IL-10-regulated ferroptosis in OPCs.

Using unbiased RNA-seq analysis, we found that the hemin-decreased *Dlk1* expression was successfully rescued by the addition of IL-10, and we further verified that STAT3 was the transcription factor for the *Dlk1* gene by using ChIP assays. *Dlk1*, also called preadipocyte factor 1 (Pref-1), is an imprinted gene that encodes for a membrane protein member of the NOTCH receptor and ligand epidermal growth factor-like protein family, mainly known for its involvement in adipogenesis [77]. With differences between in-frame deletions of the juxta-membrane protease recognition site, four isoforms of *Dlk1* are generated by alternative splicing [78]. In this study, we found that the transcription of *Dlk1* isoform 1 was primarily regulated by the IL-10/STAT3 signaling pathway and protected against OPCs lipid ROS production and subsequent ferroptosis. In line with our findings, the mammalian imprinted *Dlk1*-Gtl2 locus suppresses the PI3K-mTOR pathway and inhibits mitochondrial biogenesis, therefore protecting hematopoietic stem cells from the damage of excessive ROS production [79]. Of note, hemin treatment did not affect STAT3 activation, but decreased the expression of DLK1, suggesting that hemin modulated *Dlk1* expression in a STAT3-independent manner.

ACC, including the two isoforms ACC1 and ACC2. ACC1 is a cytoplasmic isoform that acts as a fatty acid synthesis unit, catalyzing the conversion of the acetyl-CoA to malonyl-CoA. Whereas ACC2, located in the outer membrane of mitochondria, catalyzes the production of malonyl-CoA and is an inhibitor of CPT-1 to prevent fatty acid oxidation [80,81]. Intriguingly, STAT3 activation in CD8<sup>+</sup> T cells increases fatty acid oxidation, reduces lipid ROS accumulation, and then resists ferroptosis under tumor environment [75], which implies the underlying link between STAT3 and ACC. Studies show that inhibition of ACC1/2

functions as a safeguard of ferroptosis in mouse embryonic fibroblasts [44], and DLK1 works as an inhibitory regulator of ACC1/2 in hepatocytes [45], whereas their relation in OPCs was not clear. Here, we discovered that DLK1 inhibited ACC1/2 via activation of AMPK, the most important kinase in ferroptosis [44], but how DLK1 activates AMPK is of interest for future elucidation. Polyunsaturated fatty acid (PUFA), which are substrates for synthesis of lipid signaling mediators, are susceptible to lipid peroxidation and are necessary for the execution of ferroptosis [82]. Lipidomic studies suggest that phosphatidylethanolamines (PEs), or phosphatidylcholine (PC), are key phospholipids that undergo oxidation and drive cells towards ferroptotic death [83, 84]. Consistently, in our lipidomic analysis, hemin increased the content of PUFA, and treatment with IL-10 or ND-646 modulated the lipid profile under hemin stimulation, with a decrease in PUFA-containing phospholipids. These results suggest that IL-10 protects against OPC ferroptosis by regulating lipid metabolism. Interestingly, a recent report has also shown that IL-10 reduces the lipid metabolic response of cardiomyocytes, thereby reducing inflammation and cell death in ischemia-reperfusion injury [85]. It is paradoxical that IL-10 just decreased the fatty acid (FA, 16:1), considering the role of ACC in FA synthesis and oxidation, which indicates ACC2 is the primary effector of IL-10 or there are other underlying effect pathways independent of ACC.

Whether the rescued ferroptotic OPCs successfully differentiate into myelin-producing mature oligodendrocytes is another important question for WMI recovery. We found IL-10 accelerated differentiation in naive OPCs, but not in hemin-treated OPCs, and that IL-10-rescued OPCs preserved the ability to differentiate. These data indicate that administration of IL-10 rescues OPC ferroptosis in the peri-hematoma region and may directly promote differentiation of OPCs in brain regions far from hemorrhagic damage (such as subventricular area) and these cells could migrate to the lesion and repair damaged WM.

Our study has several limitations. First, in addition to microglia, IL-10 is also released by astrocytes [86] and infiltrating peripheral immune cells (T cells [87,88] and macrophages [20]). Which cell population is the primary source of IL-10 that contributes to the improvement of WMI after ICH requires further investigation. Next, since gender is an important factor in ICH outcomes [89] and the literature has shown that IL-10 has a significant effect on anxiety-like behavior [90], it is of interest to determine whether IL-10 protects against OPC ferroptosis and improves WMI after ICH in female mice as well. Finally, administration of IL-10, AG490, and ND-646 was not specific to OPCs *in vivo*, so the protective effect in OPC ferroptosis and differentiation, and WMI may be a synergistic effect of OPCs and other cells. Thus, the development of lipid nanoparticles designed to deliver drugs precisely is a promising therapeutic strategy.

Taken together, our study is the first to demonstrate a positive effect of IL-10 on post-ICH WMI and neurologic deficits. We also found that IL-10 alleviated hemin-induced lipid ROS accumulation and ferroptosis in OPCs via the IL-10/STAT3/DLK1/ACC axis, suggesting that IL-10

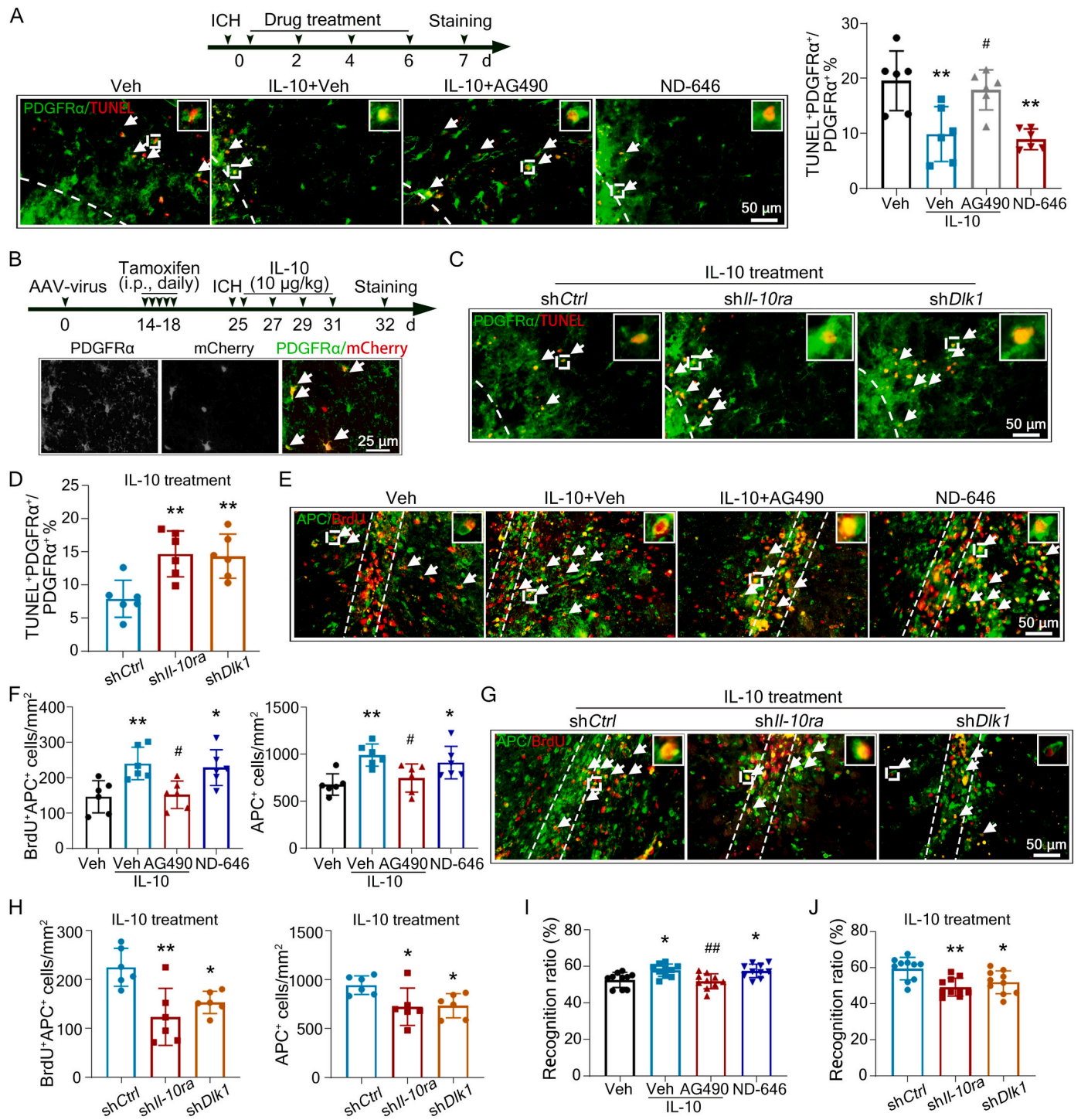


**Fig. 7.** IL-10 treatment rescues OPC ferroptosis, maintains oligodendrocytes number, and improves cognitive function post-ICH. Male WT mice (6–8 weeks old) underwent autologous intrastriatal blood injection or sham procedure (A, E, F, I). PDGFRα Cre mice (6–8 weeks old) were injected indicated AAV viruses, then underwent autologous intrastriatal blood injection (B–D, G, H, J). IL-10 in ddH<sub>2</sub>O, AG490 in 0.1% DMSO, ND-646 in 0.1% DMSO, or vehicle were infused as indicated. (A) Brain sections obtained at 7 d post-ICH were stained with PDGFRα and TUNEL. Experimental procedures, representative images and quantifications are shown. (B–D) The experimental procedures and representative images of the localization of mCherry in PDGFRα<sup>+</sup> cells are shown (B). PDGFRα and TUNEL were stained at 7 d post-ICH, and the representative images (C) and quantifications (D) are shown. (E, F) Mice were intraperitoneally injected with BrdU (50 mg/kg) twice a day for 4 d, beginning at 3 d after ICH and drug treatments were as indicated. Sections obtained at 35 d post-ICH were stained with BrdU and APC. Representative images and quantifications are shown. (G, H) After AAV-virus treatment, PDGFRα Cre mice underwent IL-10 administration. On the 3 d after ICH, mice were intraperitoneally injected with BrdU (50 mg/kg) twice a day for 4 d. Representative images and quantifications of BrdU<sup>+</sup> and APC<sup>+</sup> cells are shown. White dash lines indicate the ipsilateral hematoma area. White arrows indicate double-positive cells. (I, J) Treatments were as indicated. The performances of WT (I) or PDGFRα Cre (J) mice in novel object recognition test were quantified and shown. Results are presented as scatter plots (mean ± SD). (A, F, I) Two-way ANOVA followed Tukey's multiple comparisons test. (D, H, J) One-way ANOVA followed Dunnett's multiple comparisons test. \**p* < 0.05, \*\**p* < 0.01 vs vehicle (A, F, I) or shCtrl (D, H, J); #*p* < 0.05, ##*p* < 0.01 vs IL-10 (A, F, I). Each group contained 6 or 10 animals. Scale bars: (A, C, E, G) 50 μm, (B) 25 μm.

supplementation may be a novel therapeutic approach for the treatment of ICH.

### Author contributions

WW, ZL, FY and QL designed the research, performed most of the studies, and analyzed the data; WW, ZL, FY, and QL wrote and revised the manuscript; WW, DS, ZL, TL, ZX, ML, LH, and TS provided data acquisition, analysis and interpretation, and performed the statistical analysis; Technical and material support was provided by CZ, YW, JZ, PW and YL. All authors have agreed on the final version to be published.

### Funding

This work was supported by the National Natural Science Foundation of China [81873790 and 32070735 to Q. Li, 82271240 to F. Yang].

### Consent for publication

Not applicable.

### Declaration of competing interest

None.

### Data availability

Data will be made available on request.

### Acknowledgments

We would like to thank Dr. Xiangrong Liu (Department of National Clinical Research, Center for Neurological Diseases, Beijing Tiantan Hospital, Capital medical university) for providing the instruments of Catwalk XT® system and Dr. Zhentao Zuo (State Key Laboratory of Brain and Cognitive Science, Institute of Biophysics, Chinese Academy of Sciences) for supplying Bruker Biospin 11.7 T MR scanner.

### Appendix A. Supplementary data

Supplementary data to this article can be found online at <https://doi.org/10.1016/j.redox.2023.102982>.

### References

- [1] S.J. Dixon, et al., Ferroptosis: an iron-dependent form of nonapoptotic cell death, *Cell* 149 (2012) 1060–1072, <https://doi.org/10.1016/j.cell.2012.03.042>.
- [2] Q. Li, et al., Inhibition of neuronal ferroptosis protects hemorrhagic brain, *JCI Insight* 2 (2017), e90777, <https://doi.org/10.1172/jci.insight.90777>.
- [3] D. Shen, et al., Ferroptosis in oligodendrocyte progenitor cells mediates white matter injury after hemorrhagic stroke, *Cell Death Dis.* 13 (2022) 259, <https://doi.org/10.1038/s41419-022-04712-0>.
- [4] A.T. Hoye, J.E. Davoren, P. Wipf, M.P. Fink, V.E. Kagan, Targeting mitochondria, *Acc. Chem. Res.* 41 (2008) 87–97, <https://doi.org/10.1021/ar700135m>.
- [5] W.M.T. Jolink, et al., Location-specific risk factors for intracerebral hemorrhage: systematic review and meta-analysis, *Neurology* 95 (2020) e1807–e1818, <https://doi.org/10.1212/WNL.00000000000010418>.
- [6] M. Schrag, H. Kirshner, Management of intracerebral hemorrhage: JACC focus seminar, *J. Am. Coll. Cardiol.* 75 (2020) 1819–1831, <https://doi.org/10.1016/j.jacc.2019.10.066>.
- [7] C.W. Tsao, et al., Heart disease and stroke statistics-2023 update: a report from the American heart association, *Circulation* 147 (2023) e93–e621, <https://doi.org/10.1161/CIR.0000000000001123>.
- [8] C. Sampaio-Baptista, Johansen-Berg, H. White Matter, Plasticity in the adult brain, *Neuron* 96 (2017) 1239–1251, <https://doi.org/10.1016/j.neuron.2017.11.026>.
- [9] C. Tao, X. Hu, H. Li, C. You, White matter injury after intracerebral hemorrhage: pathophysiology and therapeutic strategies, *Front. Hum. Neurosci.* 11 (2017) 422, <https://doi.org/10.3389/fnhum.2017.00422>.
- [10] J.K. Wasserman, L.C. Schlichter, White matter injury in young and aged rats after intracerebral hemorrhage, *Exp. Neurol.* 214 (2008) 266–275, <https://doi.org/10.1016/j.expneurol.2008.08.010>.
- [11] X.R. Ma, et al., Restoring nuclear entry of Sirtuin 2 in oligodendrocyte progenitor cells promotes remyelination during ageing, *Nat. Commun.* 13 (2022) 1225, <https://doi.org/10.1038/s41467-022-28844-1>.
- [12] A.N. Bankston, et al., Autophagy is essential for oligodendrocyte differentiation, survival, and proper myelination, *Glia* 67 (2019) 1745–1759, <https://doi.org/10.1002/glia.23646>.
- [13] X. Hu, et al., Sustained ErbB activation causes demyelination and hypomyelination by driving necroptosis of mature oligodendrocytes and apoptosis of oligodendrocyte precursor cells, *J. Neurosci.* 41 (2021) 9872–9890, <https://doi.org/10.1523/JNEUROSCI.2922-20.2021>.
- [14] Q.L. Cui, et al., Oligodendrocyte progenitor cell susceptibility to injury in multiple sclerosis, *Am. J. Pathol.* 183 (2013) 516–525, <https://doi.org/10.1016/j.ajpath.2013.04.016>.
- [15] W.S. Yang, B.R. Stockwell, Ferroptosis: death by lipid peroxidation, *Trends Cell Biol.* 26 (2016) 165–176, <https://doi.org/10.1016/j.tcb.2015.10.014>.
- [16] C.D. Pandya, et al., Hemoglobin induces oxidative stress and mitochondrial dysfunction in oligodendrocyte progenitor cells, *Transl. Res.* 231 (2021) 13–23, <https://doi.org/10.1016/j.trsl.2021.01.005>.
- [17] A.R. Burmeister, I. Marriotti, The interleukin-10 family of cytokines and their role in the CNS, *Front. Cell. Neurosci.* 12 (2018) 458, <https://doi.org/10.3389/fncel.2018.00458>.
- [18] C. Jiang, et al., Immune changes in peripheral blood and hematoma of patients with intracerebral hemorrhage, *Faseb. J.* 34 (2020) 2774–2791, <https://doi.org/10.1096/fj.201902478R>.
- [19] Q. Li, et al., Microglia-derived interleukin-10 accelerates post-intracerebral hemorrhage hematoma clearance by regulating CD36, *Brain Behav. Immun.* 94 (2021) 437–457, <https://doi.org/10.1016/j.bbi.2021.02.001>.
- [20] C.F. Chang, et al., Alternative activation-skewed microglia/macrophages promote hematoma resolution in experimental intracerebral hemorrhage, *Neurobiol. Dis.* 103 (2017) 54–69, <https://doi.org/10.1016/j.nbd.2017.03.016>.
- [21] E.J. O'Neill, M.J. Day, D.C. Wraith, IL-10 is essential for disease protection following intranasal peptide administration in the C57BL/6 model of EAE, *J. Neuroimmunol.* 178 (2006) 1–8, <https://doi.org/10.1016/j.jneuroim.2006.05.030>.
- [22] S. Rodts-Palenik, et al., Maternal infection-induced white matter injury is reduced by treatment with interleukin-10, *Am. J. Obstet. Gynecol.* 191 (2004) 1387–1392, <https://doi.org/10.1016/j.ajog.2004.06.093>.
- [23] M. Sakalidou, N. Leibig, V. Boyle, G. Kouloxouzidis, V. Penna, Interleukin-10 and regeneration in an end-to-side nerve repair model of the rat, *J. Peripher. Nerv. Syst.* 16 (2011) 334–340, <https://doi.org/10.1111/j.1529-8027.2011.00368.x>.
- [24] N. Osborne, M.T. Avey, L. Anestidou, M. Ritskes-Hoitinga, G. Griffin, Improving animal research reporting standards: HARRP, the first step of a unified approach by ICLAS to improve animal research reporting standards worldwide, *EMBO Rep.* 19 (2018), <https://doi.org/10.15252/embr.201846069>.
- [25] Z. Xiao, et al., Reduction of lactoferrin aggravates neuronal ferroptosis after intracerebral hemorrhagic stroke in hyperglycemic mice, *Redox Biol.* 50 (2022), 102256, <https://doi.org/10.1016/j.redox.2022.102256>.
- [26] B.Y. Fan, et al., Liproxstatin-1 is an effective inhibitor of oligodendrocyte ferroptosis induced by inhibition of glutathione peroxidase 4, *Neural Regen Res* 16 (2021) 561–566, <https://doi.org/10.4103/1673-5374.293157>.
- [27] H.F. Yan, et al., Ferroptosis: mechanisms and links with diseases, *Signal Transduct. Targeted Ther.* 6 (2021) 49, <https://doi.org/10.1038/s41392-020-00428-9>.
- [28] H. Pu, et al., Interleukin-4 improves white matter integrity and functional recovery after murine traumatic brain injury via oligodendroglial PPARgamma, *J. Cerebr. Blood Flow Metabol.* 41 (2021) 511–529, <https://doi.org/10.1177/0271678X20941393>.
- [29] Y. Xia, et al., Tissue plasminogen activator promotes white matter integrity and functional recovery in a murine model of traumatic brain injury, *Proc. Natl. Acad. Sci. U. S. A.* 115 (2018) E9230–E9238, <https://doi.org/10.1073/pnas.1810693115>.
- [30] Z. Liu, et al., Subacute intranasal administration of tissue plasminogen activator increases functional recovery and axonal remodeling after stroke in rats, *Neurobiol. Dis.* 45 (2012) 804–809, <https://doi.org/10.1016/j.nbd.2011.11.004>.
- [31] J. Walter, et al., The CatWalk XT(R) is a valid tool for objective assessment of motor function in the acute phase after controlled cortical impact in mice, *Behav. Brain Res.* 392 (2020), 112680, <https://doi.org/10.1016/j.bbr.2020.112680>.
- [32] M. Leger, et al., Object recognition test in mice, *Nat. Protoc.* 8 (2013) 2531–2537, <https://doi.org/10.1038/nprot.2013.155>.
- [33] A.C. Geraghty, et al., Loss of adaptive myelination contributes to methotrexate chemotherapy-related cognitive impairment, *Neuron* 103 (2019) 250–265 e258, <https://doi.org/10.1016/j.neuron.2019.04.032>.
- [34] S. Tomida, et al., Usp46 is a quantitative trait gene regulating mouse immobile behavior in the tail suspension and forced swimming tests, *Nat. Genet.* 41 (2009) 688–695, <https://doi.org/10.1038/ng.344>.
- [35] K.Q. Fan, et al., Stress-induced metabolic disorder in peripheral CD4(+) T cells leads to anxiety-like behavior, *Cell* 179 (2019) 864–879 e819, <https://doi.org/10.1016/j.cell.2019.10.001>.
- [36] M. Zille, et al., Hemin-induced death models hemorrhagic stroke and is a variant of classical neuronal ferroptosis, *J. Neurosci.* 42 (2022) 2065–2079, <https://doi.org/10.1523/JNEUROSCI.0923-20.2021>.
- [37] W. Ouyang, A. O'Garra, IL-10 family cytokines IL-10 and IL-22: from basic science to clinical translation, *Immunity* 50 (2019) 871–891, <https://doi.org/10.1016/j.immuni.2019.03.020>.
- [38] H.C. Yu, et al., Canonical notch pathway protects hepatocytes from ischemia/reperfusion injury in mice by repressing reactive oxygen species production

- through JAK2/STAT3 signaling, *Hepatology* 54 (2011) 979–988, <https://doi.org/10.1002/hep.24469>.
- [39] T. Huang, et al., Construction of a novel ferroptosis-related gene signature of atherosclerosis, *Front. Cell Dev. Biol.* 9 (2021), 800833, <https://doi.org/10.3389/fcell.2021.800833>.
- [40] I. Zlatanova, et al., Iron regulator hepcidin impairs macrophage-dependent cardiac repair after injury, *Circulation* 139 (2019) 1530–1547, <https://doi.org/10.1161/CIRCULATIONAHA.118.034545>.
- [41] Y. Luo, et al., Bavachin induces ferroptosis through the STAT3/P53/SLC7A11 Axis in osteosarcoma cells, *Oxid. Med. Cell. Longev.* (2021), 1783485, <https://doi.org/10.1155/2021/1783485>, 2021.
- [42] C.W. Brown, J.J. Amante, H.L. Goel, A.M. Mercurio, The alpha6beta4 integrin promotes resistance to ferroptosis, *J. Cell Biol.* 216 (2017) 4287–4297, <https://doi.org/10.1083/jcb.201701136>.
- [43] G.A. Traustadottir, et al., The imprinted gene Delta like non-canonical Notch ligand 1 (Dlk1) is conserved in mammals, and serves a growth modulatory role during tissue development and regeneration through Notch dependent and independent mechanisms, *Cytokine Growth Factor Rev.* 46 (2019) 17–27, <https://doi.org/10.1016/j.cytogfr.2019.03.006>.
- [44] H. Lee, et al., Energy-stress-mediated AMPK activation inhibits ferroptosis, *Nat. Cell Biol.* 22 (2020) 225–234, <https://doi.org/10.1038/s41556-020-0461-8>.
- [45] Y.H. Lee, et al., Exogenous administration of DLK1 ameliorates hepatic steatosis and regulates gluconeogenesis via activation of AMPK, *Int. J. Obes.* 40 (2016) 356–365, <https://doi.org/10.1038/ijo.2015.173>.
- [46] J.Y. Lee, W.K. Kim, K.H. Bae, S.C. Lee, E.W. Lee, Lipid metabolism and ferroptosis, *Biology* 10 (2021), <https://doi.org/10.3390/biology10030184>.
- [47] B.R. Stockwell, et al., Ferroptosis: a regulated cell death nexus linking metabolism, redox biology, and disease, *Cell* 171 (2017) 273–285, <https://doi.org/10.1016/j.cell.2017.09.021>.
- [48] M.J. Joseph, J. Caliperumal, L.C. Schlichter, After intracerebral hemorrhage, oligodendrocyte precursors proliferate and differentiate inside white-matter tracts in the rat striatum, *Transl Stroke Res* 7 (2016) 192–208, <https://doi.org/10.1007/s12975-015-0445-3>.
- [49] Z. Bao, et al., Prokineticin-2 prevents neuronal cell deaths in a model of traumatic brain injury, *Nat. Commun.* 12 (2021) 4220, <https://doi.org/10.1038/s41467-021-24469-y>.
- [50] J.P. Friedmann Angeli, et al., Inactivation of the ferroptosis regulator Gpx4 triggers acute renal failure in mice, *Nat. Cell Biol.* 16 (2014) 1180–1191, <https://doi.org/10.1038/ncb3064>.
- [51] C. Beaulieu, The basis of anisotropic water diffusion in the nervous system - a technical review, *NMR Biomed.* 15 (2002) 435–455, <https://doi.org/10.1002/nbm.782>.
- [52] X. Dai, et al., TGfAlpha preserves oligodendrocyte lineage cells and improves white matter integrity after cerebral ischemia, *J. Cerebr. Blood Flow Metab.* 40 (2020) 639–655, <https://doi.org/10.1177/0271678X19830791>.
- [53] H. Johansen-Berg, V. Della-Maggiore, T.E. Behrens, S.M. Smith, T. Paus, Integrity of white matter in the corpus callosum correlates with bimanual co-ordination skills, *Neuroimage* 36 (Suppl 2) (2007) T16–T21, <https://doi.org/10.1016/j.neuroimage.2007.03.041>.
- [54] L. Wang, C.O. Leonards, P. Sterzer, M. Ebinger, White matter lesions and depression: a systematic review and meta-analysis, *J. Psychiatr. Res.* 56 (2014) 56–64, <https://doi.org/10.1016/j.jpsychires.2014.05.005>.
- [55] J. Liu, E. Likhtik, A.D. Shereen, T.A. Dennis-Tiwary, P. Casaccia, White matter plasticity in anxiety: disruption of neural network synchronization during threat-safety discrimination, *Front. Cell. Neurosci.* 14 (2020), 587053, <https://doi.org/10.3389/fncel.2020.587053>.
- [56] R.D. Porsolt, M. Le Pichon, M. Jalfre, Depression: a new animal model sensitive to antidepressant treatments, *Nature* 266 (1977) 730–732, <https://doi.org/10.1038/266730a0>.
- [57] L. Steru, R. Chermat, B. Thiery, P. Simon, The tail suspension test: a new method for screening antidepressants in mice, *Psychopharmacology (Berl)* 85 (1985) 367–370, <https://doi.org/10.1007/BF00428203>.
- [58] L. Prut, C. Belzung, The open field as a paradigm to measure the effects of drugs on anxiety-like behaviors: a review, *Eur. J. Pharmacol.* 463 (2003) 3–33, [https://doi.org/10.1016/s0014-2999\(03\)01272-x](https://doi.org/10.1016/s0014-2999(03)01272-x).
- [59] X. Lan, X. Han, Q. Li, Q.W. Yang, J. Wang, Modulators of microglial activation and polarization after intracerebral haemorrhage, *Nat. Rev. Neurol.* 13 (2017) 420–433, <https://doi.org/10.1038/nrneurol.2017.69>.
- [60] Y.B. Jiang, K.Y. Wei, X.Y. Zhang, H. Feng, R. Hu, White matter repair and treatment strategy after intracerebral hemorrhage, *CNS Neurosci. Ther.* 25 (2019) 1113–1125, <https://doi.org/10.1111/cns.13226>.
- [61] K.A. Nave, H.B. Werner, Myelination of the nervous system: mechanisms and functions, *Annu. Rev. Cell Dev. Biol.* 30 (2014) 503–533, <https://doi.org/10.1146/annurev-cellbio-100913-013101>.
- [62] B.H. Juurlink, S.K. Thorburne, L. Hertz, Peroxide-scavenging deficit underlies oligodendrocyte susceptibility to oxidative stress, *Glia* 22 (1998) 371–378, [https://doi.org/10.1002/\(sici\)1098-1136\(199804\)22:4<371::aid-glia6>3.0.co;2-6](https://doi.org/10.1002/(sici)1098-1136(199804)22:4<371::aid-glia6>3.0.co;2-6).
- [63] M. Zille, et al., Neuronal death after hemorrhagic stroke in vitro and in vivo shares features of ferroptosis and necroptosis, *Stroke* 48 (2017) 1033–1043, <https://doi.org/10.1161/STROKEAHA.116.015609>.
- [64] B.R. Stockwell, Ferroptosis turns 10: emerging mechanisms, physiological functions, and therapeutic applications, *Cell* 185 (2022) 2401–2421, <https://doi.org/10.1016/j.cell.2022.06.003>.
- [65] C. Mao, et al., DHODH-mediated ferroptosis defence is a targetable vulnerability in cancer, *Nature* 593 (2021) 586–590, <https://doi.org/10.1038/s41586-021-03539-7>.
- [66] M. Gao, et al., Role of mitochondria in ferroptosis, *Mol. Cell* 73 (2019) 354–363 e353, <https://doi.org/10.1016/j.molcel.2018.10.042>.
- [67] G. Laumet, et al., Interleukin-10 resolves pain hypersensitivity induced by cisplatin by reversing sensory neuron hyperexcitability, *Pain* 161 (2020) 2344–2352, <https://doi.org/10.1097/j.pain.0000000000001921>.
- [68] L. Pereira, et al., IL-10 regulates adult neurogenesis by modulating ERK and STAT3 activity, *Front. Cell. Neurosci.* 9 (2015) 57, <https://doi.org/10.3389/fncel.2015.00057>.
- [69] L. Song, L.F. Xu, Z.X. Pu, H.H. Wang, IL-10 inhibits apoptosis in brain tissue around the hematoma after ICH by inhibiting proNGF, *Eur. Rev. Med. Pharmacol. Sci.* 23 (2019) 3005–3011, [https://doi.org/10.26355/eurrev\\_201904\\_17582](https://doi.org/10.26355/eurrev_201904_17582).
- [70] X. Liu, et al., Glymphatic drainage blocking aggravates brain edema, neuroinflammation via modulating TNF-alpha, IL-10, and AQP4 after intracerebral hemorrhage in rats, *Front. Cell. Neurosci.* 15 (2021), 784154, <https://doi.org/10.3389/fncel.2021.784154>.
- [71] Z.S. Boyd, et al., Interleukin-10 receptor signaling through STAT-3 regulates the apoptosis of retinal ganglion cells in response to stress, *Invest. Ophthalmol. Vis. Sci.* 44 (2003) 5206–5211, <https://doi.org/10.1167/iov.03-0534>.
- [72] E. Molina-Holgado, J.M. Vela, A. Arevalo-Martin, C. Guaza, LPS/IFN-gamma cytotoxicity in oligodendroglial cells: role of nitric oxide and protection by the anti-inflammatory cytokine IL-10, *Eur. J. Neurosci.* 13 (2001) 493–502, <https://doi.org/10.1046/j.0953-816x.2000.01412.x>.
- [73] D.E. Johnson, R.A. O'Keefe, J.R. Grandis, Targeting the IL-6/JAK/STAT3 signalling axis in cancer, *Nat. Rev. Clin. Oncol.* 15 (2018) 234–248, <https://doi.org/10.1038/nrclinonc.2018.8>.
- [74] L. You, et al., The role of STAT3 in autophagy, *Autophagy* 11 (2015) 729–739, <https://doi.org/10.1080/15548627.2015.1017192>.
- [75] L. Xiao, et al., IL-9/STAT3/fatty acid oxidation-mediated lipid peroxidation contributes to Tc9 cell longevity and enhanced antitumor activity, *J. Clin. Invest.* (2022), <https://doi.org/10.1172/JCI153247>.
- [76] A.R. Hackett, et al., STAT3 and SOCS3 regulate NG2 cell proliferation and differentiation after contusive spinal cord injury, *Neurobiol. Dis.* 89 (2016) 10–22, <https://doi.org/10.1016/j.nbd.2016.01.017>.
- [77] S.B. Mortensen, et al., Membrane-tethered delta-like 1 homolog (DLK1) restricts adipose tissue size by inhibiting preadipocyte proliferation, *Diabetes* 61 (2012) 2814–2822, <https://doi.org/10.2337/db12-0176>.
- [78] C.M. Smas, D. Green, H.S. Sul, Structural characterization and alternate splicing of the gene encoding the preadipocyte EGF-like protein pref-1, *Biochemistry* 33 (1994) 9257–9265, <https://doi.org/10.1021/bi00197a029>.
- [79] P. Qian, et al., The Dlk1-Gtl2 locus preserves LT-HSC function by inhibiting the PI3K-mTOR pathway to restrict mitochondrial metabolism, *Cell Stem Cell* 18 (2016) 214–228, <https://doi.org/10.1016/j.stem.2015.11.001>.
- [80] L. Abu-Elheiga, et al., The subcellular localization of acetyl-CoA carboxylase 2, *Proc. Natl. Acad. Sci. U. S. A.* 97 (2000) 1444–1449, <https://doi.org/10.1073/pnas.97.4.1444>.
- [81] L. Chen, et al., Acetyl-CoA carboxylase (ACC) as a therapeutic target for metabolic syndrome and recent developments in ACC1/2 inhibitors, *Expert Opin. Invest. Drugs* 28 (2019) 917–930, <https://doi.org/10.1080/13543784.2019.1657825>.
- [82] W.S. Yang, et al., Peroxidation of polyunsaturated fatty acids by lipoxygenases drives ferroptosis, *Proc. Natl. Acad. Sci. U. S. A.* 113 (2016) E4966–E4975, <https://doi.org/10.1073/pnas.1603244113>.
- [83] V.E. Kagan, et al., Oxidized arachidonic and adrenic PEs navigate cells to ferroptosis, *Nat. Chem. Biol.* 13 (2017) 81–90, <https://doi.org/10.1038/nchembio.2238>.
- [84] C. Bartolacci, et al., Targeting de novo lipogenesis and the Lands cycle induces ferroptosis in KRAS-mutant lung cancer, *Nat. Commun.* 13 (2022) 4327, <https://doi.org/10.1038/s41467-022-31963-4>.
- [85] A.K. Bagchi, et al., IL-10 attenuates OxPCs-mediated lipid metabolic responses in ischemia reperfusion injury, *Sci. Rep.* 10 (2020), 12120, <https://doi.org/10.1038/s41598-020-68995-z>.
- [86] M.L. He, et al., Interleukin-10 release from astrocytes suppresses neuronal apoptosis via the TLR2/NFkappaB pathway in a neonatal rat model of hypoxic-ischemic brain damage, *J. Neurochem.* 142 (2017) 920–933, <https://doi.org/10.1111/jnc.14126>.
- [87] S.E.J. Zandee, et al., IL-10-producing, ST2-expressing Foxp3(+) T cells in multiple sclerosis brain lesions, *Immunol. Cell Biol.* 95 (2017) 484–490, <https://doi.org/10.1038/icc.2017.3>.
- [88] J. Xin, et al., IL-10 within the CNS is necessary for CD4+ T cells to mediate neuroprotection, *Brain Behav. Immun.* 25 (2011) 820–829, <https://doi.org/10.1016/j.bbi.2010.08.004>.
- [89] O. Umeano, et al., Gender and age interact to affect early outcome after intracerebral hemorrhage, *PLoS One* 8 (2013), e81664, <https://doi.org/10.1371/journal.pone.0081664>.
- [90] L. Yang, et al., Depression-like behavior associated with E/I imbalance of mPFC and amygdala without TRPC channels in mice of knockout IL-10 from microglia, *Brain Behav. Immun.* 97 (2021) 68–78, <https://doi.org/10.1016/j.bbi.2021.06.015>.